CHARACTERIZING BACKGROUND SEISMICITY IN THE REGION SURROUNDING MILFORD, UTAH

by

Stephen Austin Potter

A thesis submitted to the faculty of
The University of Utah
in partial fulfillment of the requirements for the degree of

Master of Science

in

Geophysics

Department of Geology and Geophysics

The University of Utah

December 2017

The University of Utah Graduate School

STATEMENT OF THESIS APPROVAL

The thesis of **Stephen Austin Potter**

has been approved by the following supervisory committee members:

Kristine L. Pankow	, Chair	**10/4/2017** Date Approved
Keith D. Koper	, Member	**10/4/2017** Date Approved
Peter C. Lippert	, Member	**10/4/2017** Date Approved

and by **Thure E. Cerling** , Chair/Dean of

the Department/College/School of **Geology and Geophysics**

and by David B. Kieda, Dean of The Graduate School.

ABSTRACT

A proposed site for the Department of Energy's Frontier Observatory for Research in Geothermal Energy (FORGE) is located in southwestern Utah, in the Milford Basin, west of the Mineral Mountains. This site is at the intersection of the Intermountain Seismic Belt and the Pahranagat Shear Zone. This area is known for geothermal energy and the Roosevelt Hot Springs power plant, east of FORGE, has been active since 1984. For FORGE to be successful, an induced seismicity mitigation plan is required. There have been 185 seismic events from 1850 to 2016 cataloged by the University of Utah Seismograph Stations (UUSS) in this area. In this study, I completed a noise analysis on the local seismometers IMU, NMU, and DWU and determined the capabilities for the seismic detection work. To lower the magnitude of completeness, subspace detection analysis was applied for the years 2010-2016 and the best events were relocated in a relative sense together with events from the UUSS catalog. The relocated events were analyzed through principal component analysis to determine their hypocentral geometric distribution. Within the study area, we determined a new potential fault just north of Milford, Utah and observed hypocentral geometries in the Mineral Mountains that are consistent with previously reported tectonic structures. Finally, with the additions to the UUSS catalog and completed work, we were able to complete a stability analysis to show that we successfully reduced the magnitude of completeness for the area during the time

period of 2010-2016. These results have allowed a seismicity baseline to be established for the induced seismicity mitigation plan for FORGE.

I wish to dedicate this work to those who have helped me complete this work, especially my family for enduring the hours spent completing this work.


UTAH FORGE
U.S. Department of Energy

TABLE OF CONTENTS

LIST OF TABLES

Tables

LIST OF FIGURES

Figures

ACKNOWLEDGMENTS

I would like to thank Kristine Pankow for being my chair and helping me to complete this work. I'm grateful to all my peers who have helped me along the way, namely Andy Trow, Elizabeth Pettinger, Guanning Pang, and Lisa Linville. I'm thankful for the help that Hao Zhang has provided in reviewing this work. I appreciate Keith Koper for allowing me to use his codes to complete the noise analysis. I'd also like to thank the Department of Energy for funding this project as a result of their desire to improve renewable energy production. I especially want to thank my family for putting up with the long hours devoted to this and not spending those hours with them.

CHAPTER 1

INTRODUCTION

The United States Department of Energy (DoE), in an effort to increase geothermal power production, developed the Frontier Observatory for Research in Geothermal Energy (FORGE) project. The goal of FORGE is to provide a platform in which cutting-edge research and drilling technologies may be evaluated. For FORGE to be successful, the DoE is selecting a geothermal site with specific criteria, such as an intact reservoir formation in crystalline rock with a temperature greater than 175 °C (~350 °F) at a depth of 2 km (~6500 ft). In addition to meeting the reservoir requirements, the FORGE site must undergo induced seismicity mitigation planning.

One of the two potential locations for the FORGE facilities is Milford FORGE, in west central Utah on the western flank of the Mineral Mountains (Figure 1.1, 1.2). Based on data and from the Acord-1 well (4 km west of the proposed site), the rock at depth is granitic (Moore et al., 2014) and temperatures reach 230 °C at depths of 3.8 km (Allis et al., 2015). In addition to meeting the specified depth/thermal criteria required for FORGE, the Milford FORGE site is located in an area with a long history of geothermal production: 2 km east of the Milford FORGE site is the Roosevelt Hot Springs (RHS) geothermal system. This geothermal system has been producing electricity since 1984 (Allis et al., 2012). Unlike the proposed FORGE site, RHS is a hydrothermal system in

which fluid is circulated through pathways of existing permeability.

The RHS is on the eastern edge of the Milford Valley, which is located in the Basin and Range physiographic province at the western edge of the Intermountain Seismic Belt (ISB) (Figure 1.1) (Arabasz et al., 2007). The ISB extends from Montana through central Utah and into northern Arizona (Smith and Arabasz, 1991). The Milford Valley lies on the north end of Escalante Valley, which is also the termination of the Pahranagat Shear Zone (PSZ) (Figure 1.1) (Kreemer et al., 2010). In this transition from the ISB to the PSZ, the principal stress transitions from east-west extension to a northeast-southwest shearing motion (Barker, 1986).

The Mineral Mountains, just east of the Milford FORGE site, are composed primarily of plutonic and metamorphic rocks Precambrian in age (Nielson et al., 1978). The main plutonic body of the Mineral Mountains is a syn-extensional granitic intrusion emplaced in the continental crust during the Oligocene and Miocene (Coleman and Walker, 1992). There are additional Cenozoic plutonic and volcanic rocks present in the range, particularly with Quaternary rhyolitic flows, ash deposits, and basaltic flows (Nielson et al., 1978). The north end of the Mineral Mountains is comprised of Cambrian sedimentary rocks and is overlain in places by a Cretaceous conglomerate (Sibbett and Nielson, 1980).

Volcanic activity has occurred in the area during the past 20 Ma to 30 Ma (Barker, 1986). The youngest volcanism dated began 0.8 Ma and is located 4 km east of the Roosevelt Geothermal System (Figure 1.2). This volcanic activity continued along the western flank of the Mineral Mountains until ~0.5 Ma (Ward et al., 1987). The magma intrusions underneath the Mineral Mountains may have contributed to the surface uplift

of the mountains (Nielson et al., 1986). The topography in the Mineral Mountains appears old and the Oligocene plutonic rocks are strongly weathered to gruss, suggesting the surface has been exposed for a significant amount of time (i.e., not an active landscape). Beneath the Mineral Mountains at a depth of approximately 15 km is a low seismic velocity body that is consistent with the presence of partial melt, and may be a potential heat reservoir for the geothermal system (Figure 1.2) (Robinson and Iyer, 1981).

Multiple north-south and east-west structures have been mapped in the region surrounding the Milford FORGE site (e.g., Sibbett and Nielson; 1980, Brogan and Birkhahn, 1982; Nielson et al., 1986, 1978). The main structures (Figure 1.2) of interest are the north-south striking Opal Mound (Dome) fault located to the east of the FORGE site (Nielson et al., 1978), the east-west striking Negro Mag fault located to the northeast of the FORGE site (Nielson et al., 1978), and the West Mineral Mountain fault located south of the FORGE site in the Milford basin (Brogan and Birkhahn, 1982; Smith and Bruhn, 1984).

The Opal Mound fault is a normal fault that dips steeply to the east in the direction of the Mineral Mountains and not towards the basin as is typical for Basin and Range range bounding faults (Brogan and Birkhahn, 1982). The Negro Mag fault is an east-west structure that is dipping steeply towards the south at approximately 80° shallowing to a dip of 65° at a depth around 250 m. This fault has a subtle morphological expression (Brogan and Birkhahn, 1982) but is evident by offset dikes reported by Nielson et al. (1978). These dikes are steeply dipping in the northern portion of the Mineral Mountains but are sub-horizontal on the southern end. This is likely due to the tilting that occurred during formation of the Beaver Valley and Cave Canyon detachment

fault approximately 8-9 Ma (Coleman and Walker, 1994). The Beaver Valley and Cave Canyon detachment faults are north-south trending listric normal faults that dip towards the west with the Cave Canyon fault joining the Beaver Valley fault at depth. The Mineral Mountains West fault dips west and may sole into a large low-angle normal fault (Smith and Bruhn, 1984).

Structural complexity is important in controlling boundaries and geothermal reservoir characteristics (Faulder, 1991). For example, the east-west trending Negro Mag is a cross fault of the Opal Mound fault towards the west and together they form permeability structures important to the hydrothermal system at RHS (e.g., Allis et al., 2012). The exact relationship of how these two faults meet is poorly understood. No fluid injected from the RHS power plant on the west of the Opal Mound fault returns to the system. The Negro Mag fault also appears partially or wholly impervious to fluid migration and an additional tracer analysis study is being conducted to confirm this observation (Rob Toler, personal communication).

Looking beyond the Milford FORGE site, the largest earthquake recorded in the area was a M 4.1 event (based on intensity) in 1908 (Figure 1.2) (Arabasz et al., 2016). A moment tensor solution for a more recent event (April 10, 1998), located north of Milford (Figure 1.2) but close to the 1908 event, indicates steeply dipping strike-slip movement (Whidden and Pankow, 2012). Further analysis of the University of Utah Seismograph Stations (UUSS) earthquake catalog for this area from 1850 through the present indicates low seismicity rates and low magnitudes. In fact, there was no seismicity recorded in the catalog east of Milford through the Mineral Mountains for 2011-2016.

To improve fault location and orientation, as well as to better assess the potential

for induced seismicity, a seismic survey was conducted in advance of development of the RHS power plant (Zandt et al., 1982). This survey consisted of six short-period seismic stations located on the western flank of the Mineral Mountains. Elements of the seismic array were installed from January 1979 to January 1982. During this experiment, only one significant sequence of earthquakes was observed from June 27 through August 28, 1981. The observed seismic swarm consisted of 1044 earthquakes, of which 686 were locatable. The largest earthquake in the swarm was M 2.0. Most events located east of the seismic array (Figure 1.2) and had depths of 4-5 km. Zandt et al. (1982) concluded that the swarm was due to natural fluid migration and most likely not caused by geothermal production. They also concluded that the region is characterized by few earthquakes and small magnitude events punctuated by seismic swarms.

The goal of this study is to test the last conclusion of Zandt et al. (1982) by carefully detailing the background seismicity to determine rates, magnitudes, and locations relative to the known geologic structures. This analysis is essential to designing an informed and rigorous induced seismicity mitigation plan for the Utah FORGE site. Specifically, I completed a noise analysis of UUSS stations IMU, NMU, and DWU, located within 45 km of the Milford FORGE site, in order to determine event detection quality (Ch. 2). I then describe and apply a protocol to ascribe earthquakes in the UUSS catalog to natural or anthropogenic seismic sources (Ch. 3). I used subspace detections on the continuous data from stations IMU, NMU, and DWU to enhance the UUSS catalog for the time period 2010-2016 in the Milford, Utah region in order to reduce the magnitude of completeness (the minimum magnitude in which all events above this threshold are reliably recorded) (Ch. 3). Detected events were located using established

relative relocation algorithms (Ch. 4). These event locations then were used to determine fault geometry using principal component analysis (Ch. 5). I used this procedure to build a more robust seismic catalog and show more of the complexity of the faulting in this region. These results also provide the necessary baseline of historical seismicity required by the FORGE project, for safe operation of the facility.

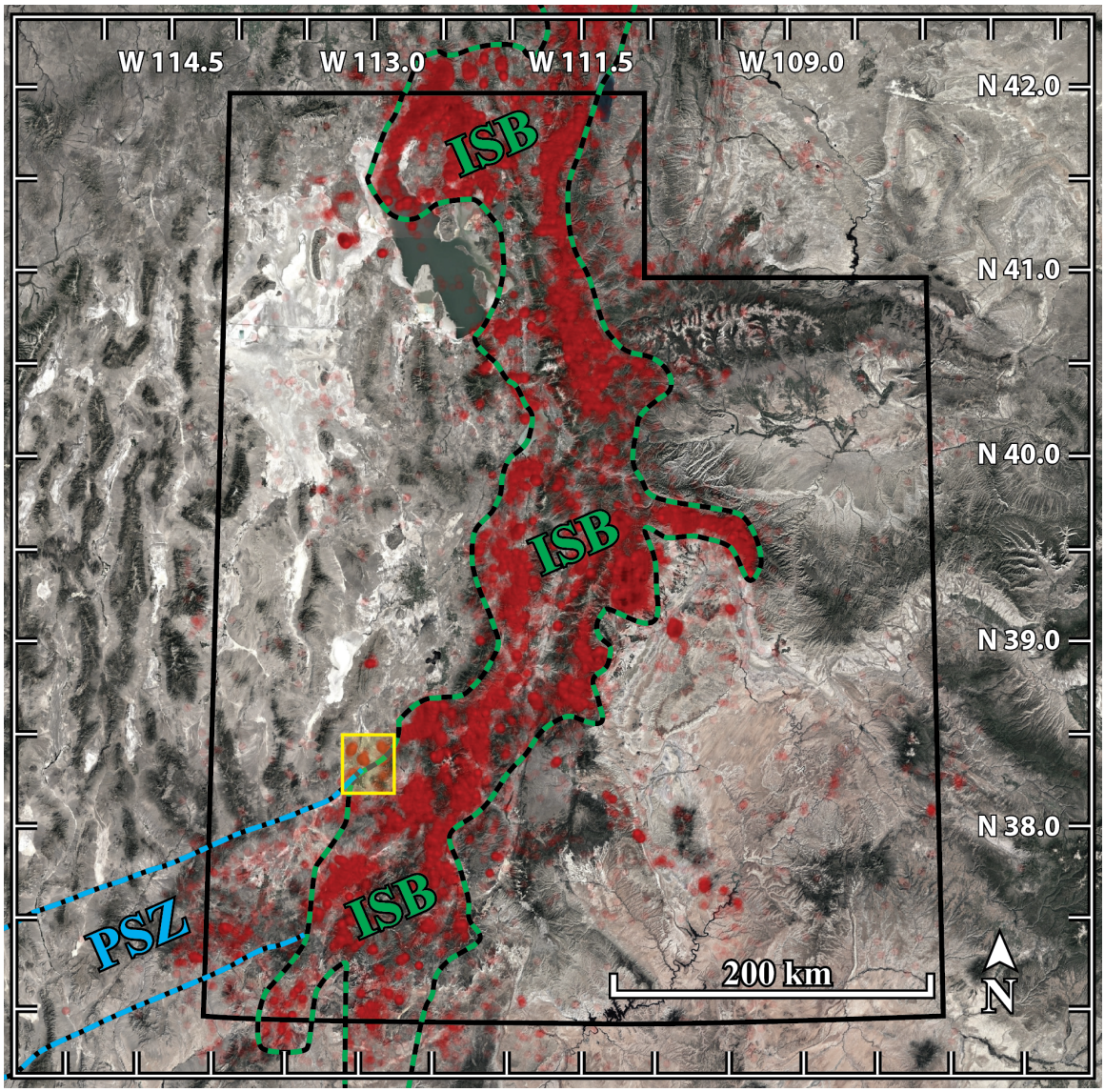

Figure 1.1. Overview of seismicity in Utah for 1850-2016 (red circles). State of Utah (black outline). The Intermountain Seismic Belt (ISB) is denoted by the green and black dashed line. The outline denotes a majority of the earthquakes occurring in the ISB. The Pahranagat Shear Zone (PSZ) is outlined with a blue and black dashed line. The yellow box denotes the area shown in Figure 1.2 where Milford, Utah, and the FORGE site are located. Imagery from Google Earth.

Figure 1.2. Seismicity (red circles) near Milford, Utah (white square) for 1850-2016. Green star represents epicenter of largest earthquake in study area, 1908 M4.1. The blue triangles represent the seismic stations used in this study, labels on figure. The black rectangular outline represents the study area. The pink shape with dashed outline is the footprint of the local windfarm. The green polygon is the proposed FORGE footprint. The black dashed lines represent major faults in area; Opal Mound (OP), Negro Mag (NM), and West Mineral Mountain (MW). Roosevelt Hot Springs (RHS) is denoted by white circle with black outline. Yellow filled shapes represent recent (0.8 Ma - 0.5 Ma) volcanism (Ward et al., 1987). Light blue filled shape represents the areal extent of an earthquake swarm reported by Zandt et al. (1982). White outline represents low seismic velocity area (Robinson and Iyer, 1981). Moment tensor from April 10, 1998 M 3.91 seismic event (Whidden and Pankow, 2012). Imagery from Google Earth.

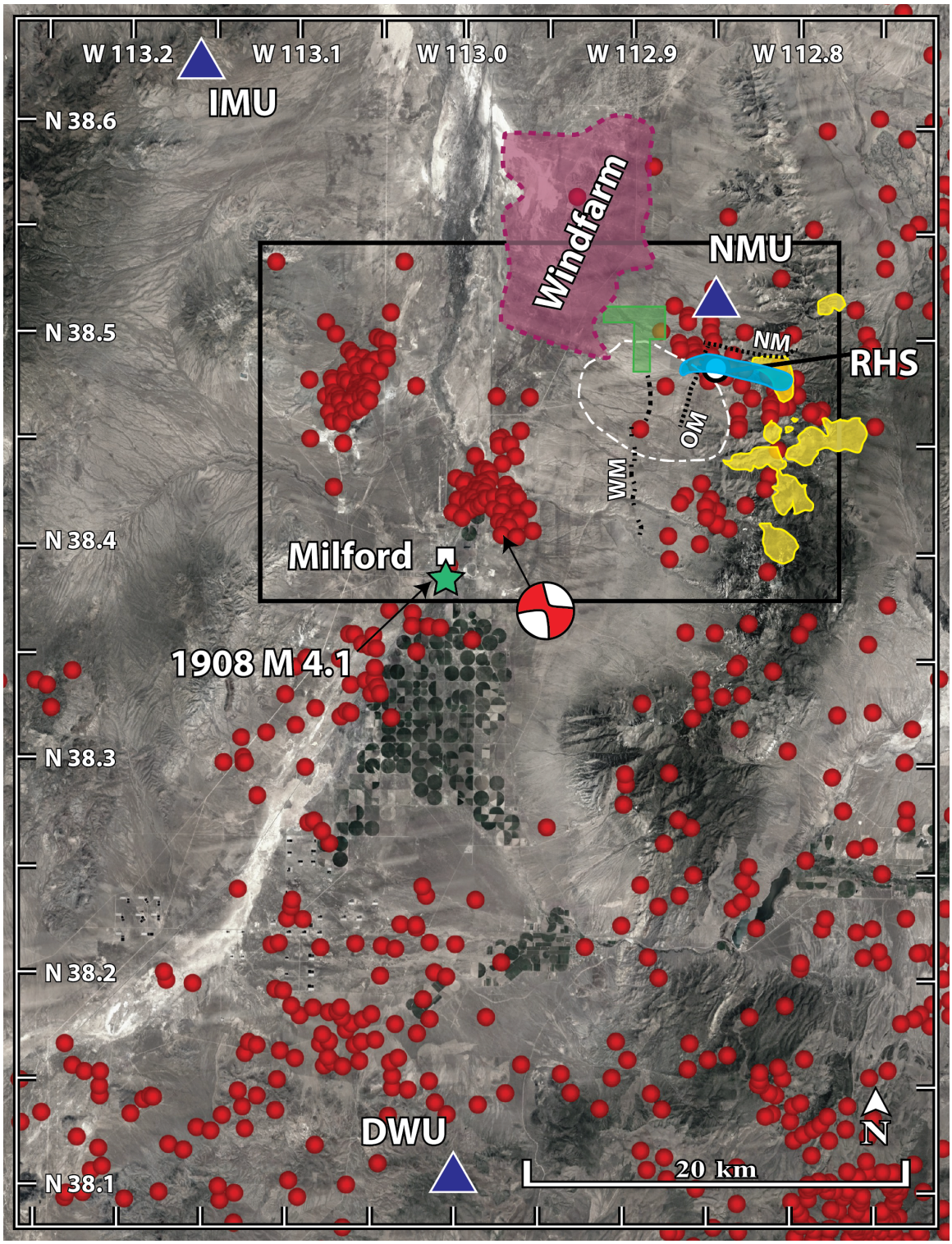
W 113.2
W 113.1
W 113.0
W 112.9
W 112.8
IMU
N 38.6
N 38.5
N 38.4
N 38.3
N 38.2
N 38.1
Windfarm
NMU
NM
RHS
OM
WM
Milford
1908 M 4.1
DWU
N
20 km

CHAPTER 2

NOISE ANALYSIS

One goal of this research was to detect smaller magnitude events and thereby decrease the magnitude of completeness (M_{comp}), which is a function of the Signal-to-Noise Ratio (SNR) at the nearby stations and network geometry. To achieve this goal, the noise quality of stations in close proximity to the study area was assessed. A noise analysis of the stations allowed the review of noise levels (amplitudes) within various frequency bands of interest. Those frequencies with low noise lend credibility to the ability of a station to detect low amplitude signals within those frequencies containing low noise. To review the noise levels at stations IMU, NMU, and DWU, I completed a power spectral density (PSD) analysis which I describe below.

Power spectral density is a signal-processing technique that evaluates the power distribution of a continuous time series with respect to frequencies via a Fast Fourier Transformation (FFT). Power at these frequencies is reported in Decibels (dB), equation 2.1,

$$Decibels\ (dB) = \left(10 * \log_{10}[\frac{Input}{1\frac{m}{s^2}}] \right) \tag{2.1}$$

where $Input$ is the resulting Fast Fourier Transform value ([meters/second^2]^2/Hertz) (Heinzel et al., 2002; McNamara and Buland, 2004). The resulting dB can then be

compared with high and low reference noise models (Peterson, 1993).

2.1 Data

Continuous vertical-component seismic data for UU regional stations NMU, IMU, and DWU (Figure 1.2) were retrieved from Incorporated Research Institutions for Seismology: Data Management Center (IRIS DMC) using web-services. The data were requested in one-hour-long segments for the chosen time ranges and saved in Seismic Analysis Code (SAC) format, with the accompanying station response files. Data for stations NMU and DWU were retrieved for 2014 though 2016 and IMU data were retrieved for 2007 through 2016 to provide a longer window of continuous data for further analysis described below.

2.2 Power Spectral Density Analysis

Power spectral processing followed the methodology of Koper and Burlacu (2015). First, the data were detrended. Then, the instrument response (the influence on the signal due to the seismic instrumentation) was removed, and the data transformed to ground acceleration using a trapezoidal frequency domain filter defined by frequencies of 0.01 Hz to 0.05 Hz and 25.0 Hz to 50.0 Hz to focus within the frequencies generated by earthquakes. For the acceleration waveforms, the mean was removed and then filtered using a Nuttall4c taper (Heinzel et al., 2002). The Fast Fourier Transformation (FFT) was applied using a window length of 819.2 seconds with a 50% overlap. At the end of this procedure, each one-hour-long segment was saved with frequency in Hertz (Hz) and power in decibels (dB), as expressed in equation 2.1.

2.3 Results

Initial PSD plots for all three stations for the year 2015 show that microseismic noise, defined as noise between frequencies of 0.1-0.5 Hz, is most prominent during winter months (Figure 2.1). Peak power in the 1-10 Hz range of the spectrograms varies in frequency and intensity as a function of time (Figure 2.2A). A sinusoidal trend is visible on IMU between 1 Hz and 5 Hz. A similar trend is visible on NMU in the 3-5 Hz passband and at 10.2-0.5 Hz (Figure 2.2B). For DWU, however, extremely high noise is present across multiple frequencies over a period of many hours to days with no visible sinusoidal trend (Figure 2.2C).

To further analyze the properties of the sinusoidal signal observed in the IMU and NMU station data, the time range of the continuous data was expanded to include the years 2014 and 2016. The sinusoidal pattern observed in IMU data remains prominent over this longer study interval and is visible in the 1 Hz and 5 Hz range (Figure 2.3A). At NMU, a sinusoidal trend is most prominent at 10.2-10.5 Hz, but it is also less prominently observed between 3-5Hz (Figure 2.3B). Similar to the one-year data, the signal is not evident at DWU over the longer time range (Figure 2.3C).

More in-depth analysis of this sinusoidal pattern at IMU from 2014-2016 shows that the minima power occurs during the months of April 2014 and 2015 and May 2016, with the maxima occuring in August 2014 and October 2015 and 2016 always at 5.5-6 Hz (Table 2.1). Looking in short time windows, it is evident that the sinusoid is composed of three distinct bands of energy (Figure 2.4). As the frequency increases, the in-phase energy converges, and the signal is greatest at the maxima. During the shifts toward lower frequencies, the three frequencies diverge, with the greatest divergence observable

at the minima.

There are two other notable bands of power visible in the IMU spectrogram: (1) from approximately 9.7 Hz to 10.5 Hz and (2) from approximately 10.2 Hz to 10.9 Hz (Figure 2.5). These power bands follow the same sinusoidal pattern as in the 1-6 Hz frequency band.

2.4 Windfarm Contribution

Neither the site location, nor the instrument themselves, contribute to the observed sinusoids. IMU is located on the surface and NMU within a mineshaft, suggesting that temperature variations at the instrument or specific site conditions do not contribute to the sinusoid trend. A potential cause of the sinusoidal-like signal is the nearby windfarm (Figure 1.2). Wind power generators can generate noise in the 1-10 Hz frequency band (Bowers et al., 2015; Estrella et al., 2017). The primary bending mode of a turbine with fixed rotors is 1.7 Hz with secondary bending modes at 10.5 Hz and 10.9 Hz (Prowell et al., 2010). These are the approximate frequencies observed in the spectrograms from IMU and NMU from January through June. In order to test if the windfarm contributes to the observed signal, data from IMU for the dates bounding the official start date (November 2009) of the Milford Windfarm (SCPPA, 2017) were analyzed. The first wind turbine was completed June 29, 2009 and a total of 97 turbines were completed by the end of 2009; a total of 165 turbines were completed by the end of 2011.

To better understand a potential noise contribution from the windfarm, station IMU data from 2007 (two years before the first turbine installation) through 2016 were

analyzed (Figure 2.6). Unfortunately, there is a data gap from August 2009 through March 2010. For the months prior to the data gap, and prior to the installation of the first turbines, the sinusoidal pattern is not obvious. Between the completion of the first phase (2009) and second phase (2011) of wind tower construction, the sinusoidal-like pattern is present but difficult to discern due to many hours of high noise (Figure 2.6). It is unclear what contributed to the high noise during this time. The sinusoidal-like signal becomes prominent after all wind towers are in operation and the station's noise levels reduce. Estrella et al. (2017) determined that it took multiple wind towers (5) to project a signal over 11 km. IMU is at a distance of 16 km from the windfarm.

While the wind farm can explain the frequencies observed, it does not account for the yearly shift in the observed peak frequency. The peak frequency variation correlates with measured change in temperature recorded at the MesoWest weather station located at the Milford airport 25 km away (Figure 2.7). The peak correlation has a time lag of 23 to 77 days depending on the year (Table 2.2). Possible explanations for this correlation with temperature include windfarm operation changes (e.g., throttling turbine rotation, locking turbines, stalling turbines, and changing facing direction of the turbine). Another potential explanation for the frequency shift lag due to temperature change is thermoelastic strain (Tsai, 2011; Ben-Zion and Allam, 2013). However, the correlation at IMU and NMU is inverse to those observed in the thermoelastic strain observations. According to thermoelastic strain, it would be expected that the frequencies would increase during the winter and decrease during the summer months, after the observed lag. This is not the case for the observed signal at IMU and NMU. While temperature

seems to be related to the change in frequency, the actual mechanism of this change is outside the scope of this project and is a potential area for further research.

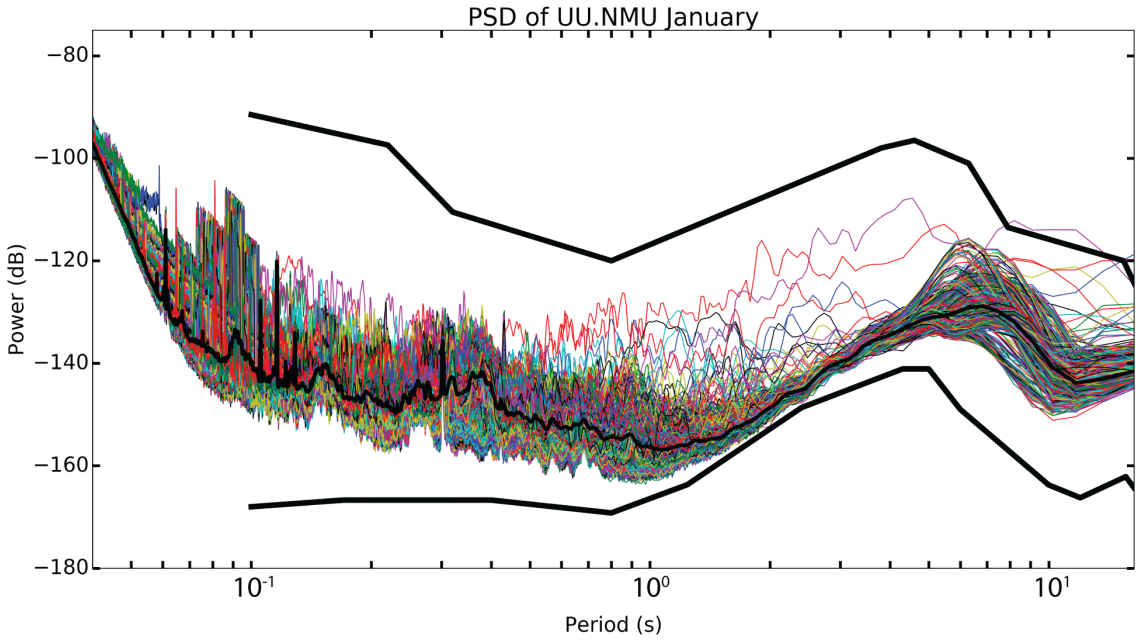

Figure 2.1. PSD of noise for station NMU during the month of January 2015 plotted by individual hour. The thick black line in the middle is the mean of all the hours. The bounding black lines represent the high and low noise models (Peterson, 1993). Note that the microseism band is visible in the 2-10 second period range.

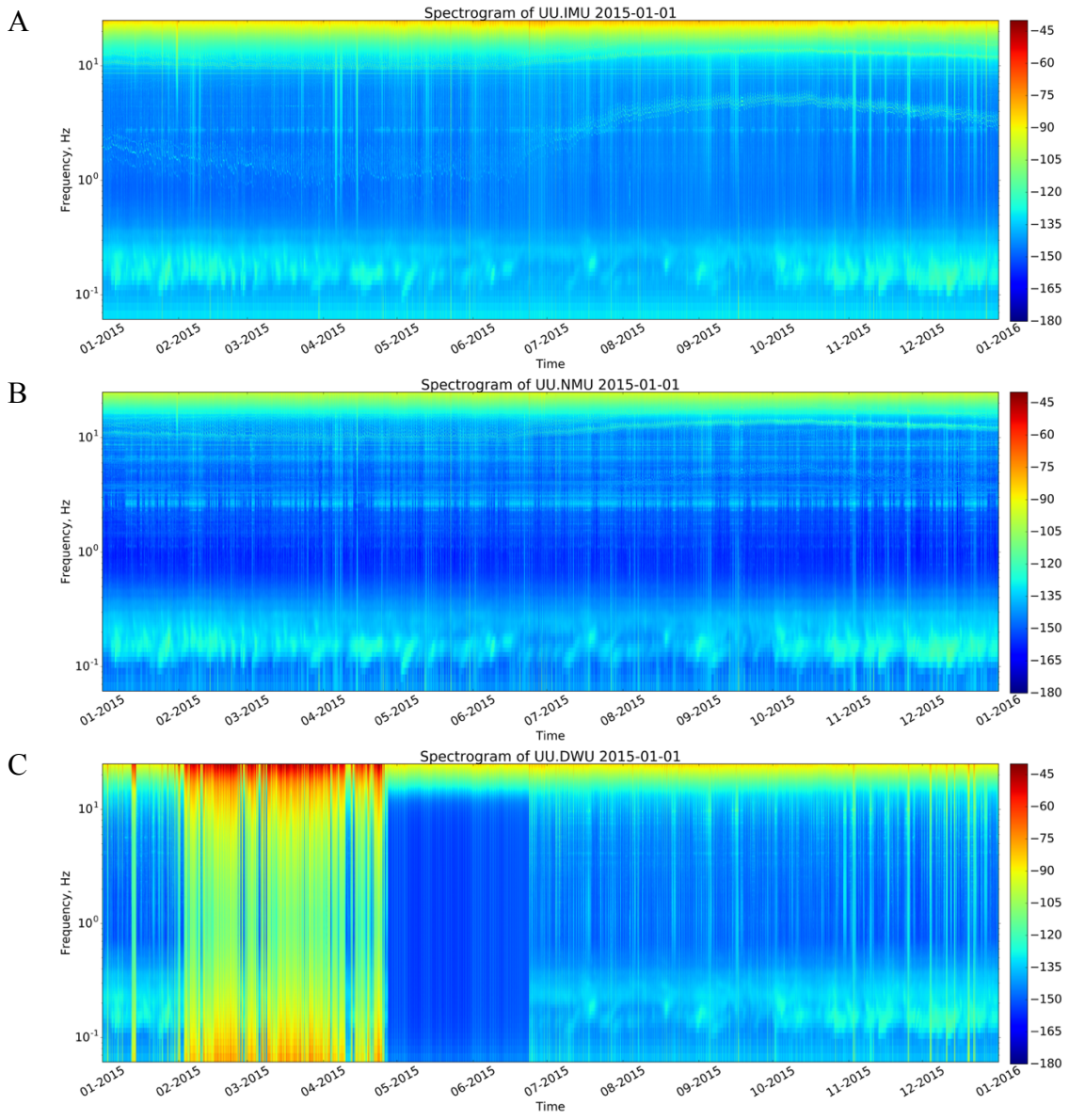

Figure 2.2. The spectrograms of IMU (A), NMU (B), and DWU (C) for 2015. Individual hours are plotted together with color representing the power in dB. DWU shows poor data quality during the months of February through June. Microseisms are visible in the 0.5 to 0.1 Hz range with the highest power during the winter and early spring. If an hour was missing in the dataset, then its power values were continued until the next hour of available data.

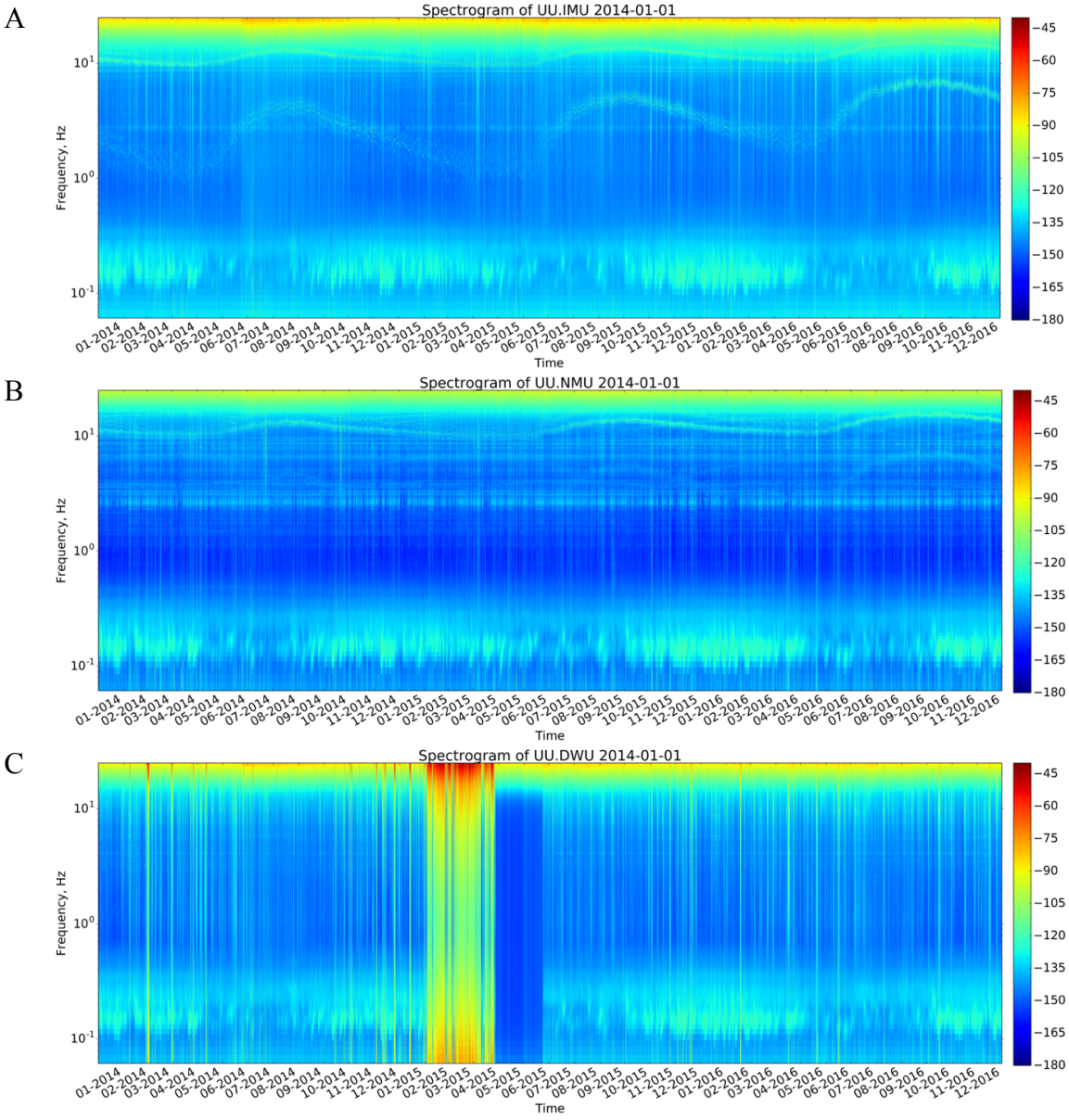

Figure 2.3. The spectrograms of IMU (A), NMU (B), and DWU (C) for 2014-2016. Individual hours are plotted together with color representing the power in dB. While no visible yearly trend (outside the microseism) is visible in DWU, NMU and IMU, both show strong sinusoidal-like signals that show sub-annual variations. If an hour was missing in the dataset, then its power values were continued until the next hour of available data.

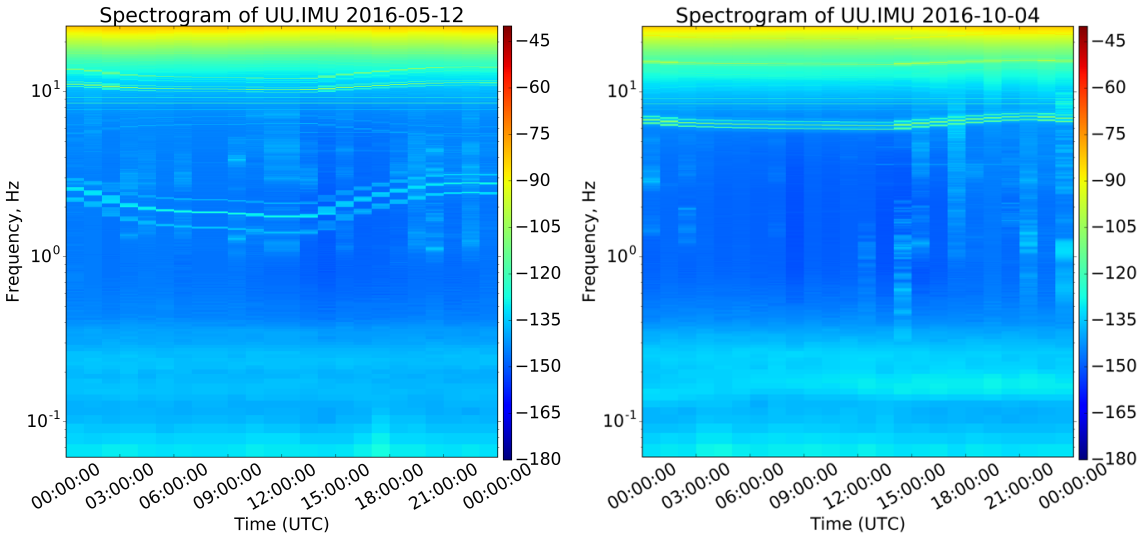

Figure 2.4. Spectrograms showing 24-hour segments for IMU during two different days of the year; May 12, 2016 and October 4, 2016. Note the three bands of in-phase high-power frequencies. The spectrogram on the left shows the frequency around 1.5 Hz and the one on the right approximately 5.5 Hz. Both show a diurnal variation with frequencies increasing following daylight hours.

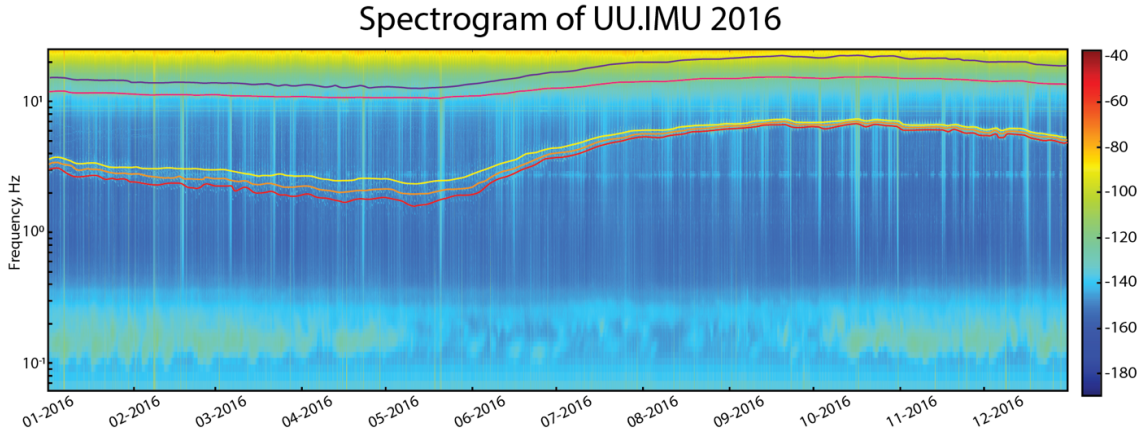

Figure 2.5. Spectrogram for year 2016 for station IMU. In order to more clearly show the signal that can be seen at IMU, the signals of interest have been highlighted with solid lines for the year 2016. There are five visible signals in these data that show a roughly in-phase sinusoidal-like pattern with yearly variation. Note that as the lower three frequencies increase through time, they converge and then diverge as the frequency drops. If an hour was missing in the dataset, then its power values were continued until the next hour of available data.

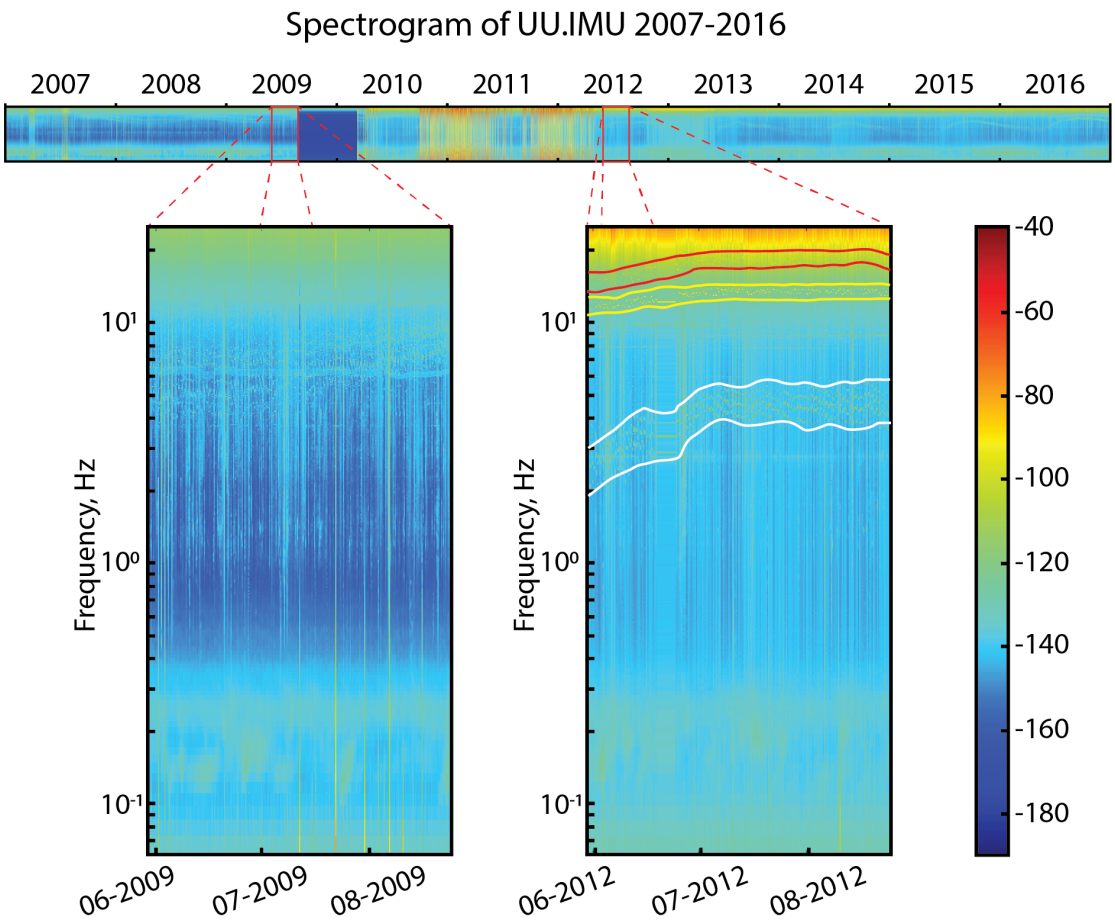

Figure 2.6. Spectrogram of IMU for years 2007-2016. The two zoomed-in areas show the signal pre-construction (left) and post-construction (right) of the Milford windfarm. White, yellow, and red lines bound frequencies 2-5 Hz, 10.2 Hz, and 10.5-10.7 Hz, respectively. The station gain increased for IMU in April of 2010 and is the reason for the visible difference in power between the two time periods of interest. There is a gap in the data (not a period of low noise) from August 2009 until March 2010. If an hour was missing in the dataset, then its power values were continued until the next hour of available data.

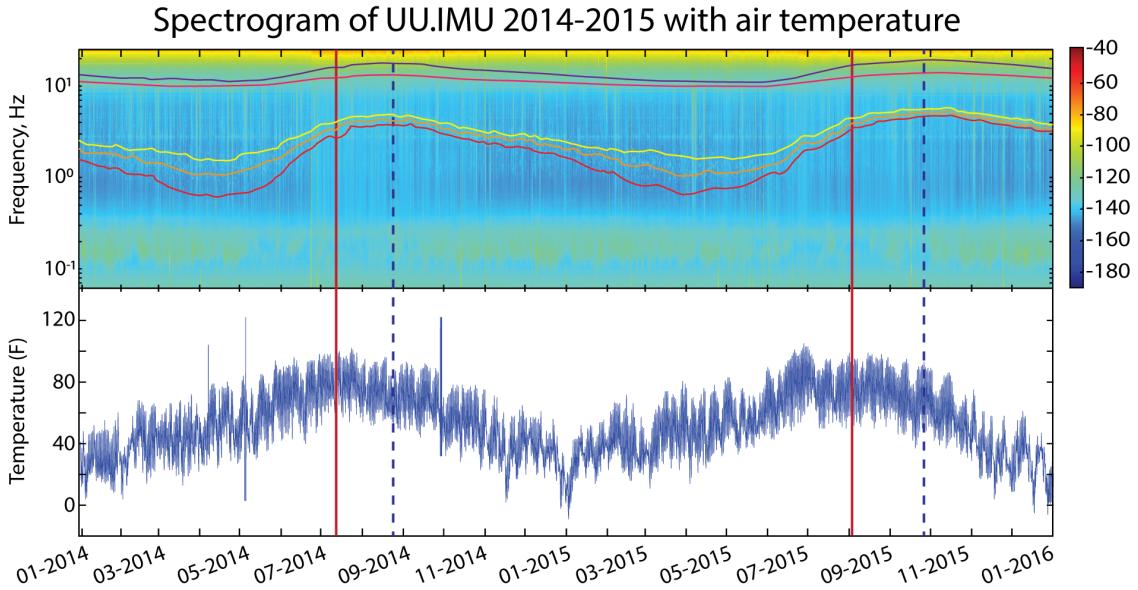

Figure 2.7. Spectrogram of IMU with corresponding weather data for years 2014 and 2015. The red lines indicate the approximate peak of air temperature for each year. The blue dashed lines indicate the peak frequencies in the observed signals. Notice that the delay between the two years is not identical, with an approximate delay of 41 days in 2014 and 51 days in 2015. If an hour was missing in the spectrogram dataset, then its power values were continued until the next hour of available data.

Table 2.1. Power maximums and minimums for the sinusoidal trends for each year and the month in which they occurred with their corresponding frequencies.

	Maximum		Minimum	
2014	August	~5.5-6	April	~1
2015	October	~5.5-6	April	~1
2016	October	~5.5-6	May	~1
	Month	Frequency, Hz	Month	Frequency, Hz

Table 2.2. Lag periods for peak frequency of the 1-6 Hz sinusoid with peak temperature.

Year	Lag (days)
2013	23
2014	41
2015	51
2016	77

CHAPTER 3

CATALOG DISCRIMINATION AND ENHANCEMENT

The magnitude of completeness for the University of Utah Seismograph Stations (UUSS) in the Milford Valley is ≥ 1.7 (Pankow et al., 2004). However, the study conducted by Zandt et al. (1982), using a temporary local array, detected swarm activity that was principally composed of earthquakes $M < 1.5$. To better understand seismicity in the region and to determine if there are many uncatalogued small magnitude earthquakes, we enhance the UUSS catalog using a subspace detection algorithm (Harris, 2006; Harris and Paik, 2006, Barrett and Beroza, 2014; Chambers et al., 2015), which has greater resolving power for detecting events with similar locations and mechanisms than more standard matched filter techniques that use single event waveforms (e.g., Schaff and Waldhauser, 2005; Pankow et al., 2014) or stacked waveforms (e.g., Gibbons and Ringdal, 2006; Plenkers et al., 2013).

Subspace detection uses Singular Value Decomposition (SVD) to decompose a family of similar events into basis vectors. Barrett and Beroza (2014) suggest that the first two basis vectors represent the average waveform and time derivative of the average, respectively. Using the basis vectors, events with subtle changes in location and mechanism to the original family of events can be detected. In the following analysis, we follow the implementation of subspace detection from Chambers et al. (2015) and use the

Detex software program (v 1.0.8) (Github: https://github.com/d-chambers/Detex).

3.1 Data

Earthquakes from the UUSS catalog (1976-October 2012, Stein, 2016; October 2012-2016, USGS Comcat) from 1976 through 2016 for the Milford, Utah study area (184 events) fall into 3 distinct geographic regions (Figure 3.1): (1) Mineral Mountains (MM); (2) immediately northeast of Milford, near the airport (AP); and (3) northwest of Milford near an area with quarries (QR). For these regions, there are 58, 65, and 61 events, respectively. Since we are primarily interested in an earthquake catalog, it is important to determine if events located in the QR area are natural or are related to mining activity such as blasting. A useful discriminator for distinguishing blasts is the time of day. Utah law requires that all blasts be completed during daylight hours. The origin times for QR events were plotted against the hour in the day in which they occurred (Figure 3.2). All events occurred during daylight hours, supporting the influence that these are mining-related events. In addition to the time of day, the median depth for the 61 events in the QR area is 2.0 km with a median error of ± 3.4 km, suggesting shallow sources. The waveforms from the QR boundary also lacked a clear P- and S-wave. Based on these observations, we classified these events as anthropogenic and removed them from further analysis.

The remaining AP and MM region were then analyzed for waveform quality, and available P-arrival times for stations IMU, NMU, and DWU were collected. The catalog events were compiled into a list of template events. To construct the template event keys for each region, two-minute waveform snippets for the template event-station pairs were

retrieved from the Incorporated Research Institutions for Seismology Data Management Center (IRIS DMC) Web Services beginning at the origin time. Each waveform was manually reviewed to determine good signal-to-noise and clear P and S energy. Those events that had poor waveform quality were removed from their respective region. This quality review reduced the number of MM events to 43 with magnitudes ranging from 0.52 to 2.39 M_L in the time span of 1993 through 2011. The AP data set was reduced to 56 usable events with magnitudes of 0.46 to 3.91 M_L with a time range spanning 1995 to 2001. These cataloged events were used to create separate template keys for each region for the subspace detection. Not all events were well recorded on all three stations.

We also downloaded continuous data for the vertical component for stations IMU, NMU, and DWU retrieved in hour-long segments from IRIS DMC Web Services for years 2010-2016. All continuous data were quality controlled by sampling rate, time range retrieved, empty channels, and numbers and durations of data gaps. Hour-long segments with incomplete data or problems with sampling rates were removed from further use.

3.2 Clustering

The first step of subspace detections includes identifying families of similar events. This is accomplished by cross-correlating all event waveforms at each station and then using single-link clustering to build event families. Single-link clustering builds a family by first linking events that most closely resemble one another. It then moves towards more dissimilar waveforms and groups those with previously clustered waveforms. Moving through the waveforms, families are continuously created based on

their level of similarity. Ultimately, all the events link into a single family at the furthest point of similarity.

Two parameters are needed for clustering: the window length used to define how the signal should be cut to contain the most pertinent information, referred to as the trim window, and the minimum cross-correlation coefficient to define waveform similarity. The trim window proved to be very important. If the trim window is too large, then a mismatch of phases may occur and/or long windows of noise may be included. If the window is too short, then there is not enough information in the waveforms to distinguish families. For this analysis, the trim window length is the same for all stations and starts 2 seconds before and continues 25 seconds after the P-arrival. This window length was found to be adequate for both the AP and MM regions as it captured the P- and S-wave energy from all three stations. Cross-correlation coefficients were used to determine at what point clusters should be split. As the waveforms from each station differed, so too did the clustering. Different cross-correlation coefficients were used to split the clustering on all stations to a similar number of clusters and number of events within each cluster. The cross-correlation coefficients used were 0.650, 0.650, and 0.700 for stations NMU, IMU, and DWU, respectively in the MM region. The cross-correlation coefficients used for the AP region were 0.875, 0.880, and 0.865 for stations NMU, IMU, and DWU, respectively.

Before cross-correlation is performed, the instrument response is removed and the data filtered from 1-10 Hz. Figure 3.3 shows results of the clustering and the resulting families for each station and region. Events in the AP region separated into 7 to 10 families and the MM separated into 9 to 11 families. The clusters created for each station

did not always consist of the same events (e.g., events A and B but not C clustered on station 1, but events B and C and not A clustered on station 2). For both regions, there are events that did not sufficiently correlate with other events to form families. These events are referred to as singletons and are used in a traditional cross-correlation approach to derive more events.

To assess the clusters distribution spatially, the hypocenters, event times and waveforms from the clusters were plotted in Google Earth (Figure 3.4). Thus, we quickly determined if the clustered events shared similar locations and distances between events of the same family. This allowed rapid visual assessment of suitable cross-correlation values.

3.3 Subspace Detection

In order to create subspaces based on the clustered events, waveforms were aligned along the P-arrival time (Figure 3.5). These waveforms were then trimmed to match the trim window length used in clustering. Singular Value Decomposition (SVD) was performed to calculate the orthonormal basis vectors. The energy that each basis vector contributes to describing the event family, called fractional energy, was calculated. While any choice of fractional energy may be used, we required that there be enough basis vectors included in the subspace to capture 90% of the total energy (Figure 3.5). The first basis vector is the average waveform of the cluster and the second represents its time derivative (Barrett and Beroza, 2014). Subsequent vectors have no clear physical representation of the cluster. We parameterized the cluster space such that 3 or fewer basis vectors were needed to describe 90% of the fractional energy (Figure 3.5).

For each resulting subspace, a detection threshold is required to determine at what point a detection would be triggered. We accomplished this by analyzing 100 hours of continuous data for each subspace-station pair. Only hours that have no potential large seismic signals were used in this process (large signals being defined as an hour of continuous data with signals above eight times the root-mean-square amplitude). A beta distribution was fit to the detection statistic through the maximum likelihood method. The detection threshold was set to the upper tail of the beta distribution, reducing the likelihood of a false detection to 10^{-12} (Chambers et al., 2015).

3.4 Results

The subspace and singleton detections identified a total of 409 events for the AP region using the criteria that a minimum of two stations are required per detection. The detections were filtered from 1-10 Hz and compared to the template events. In some cases, because of the length of the trim window, phases were mismatched when compared to the templates. In other cases, the templates detected either events with poor signal-to-noise or pure noise. For both cases, these detections were removed. Following this quality control step, there were 9 detections remaining in the AP region, with magnitudes ranging from -1.49 to 0.91, occurring from 2011 through 2016 (Figure 3.6). The magnitudes are calculated through Detex based on the template events that led to their detection.

Using the subspaces and singletons for the MM region, there were 499 events identified using a minimum of two stations to be required per detection. These events were filtered from 1 Hz to 10 Hz and compared to the MM template events. Detections

that were misaligned on phases, had poor signal-to-noise, or had pure noise were removed. This revised the MM dataset to 61 detected events with magnitudes ranging from -0.55 to 1.52, with events spanning 2011 through 2016 (Figure 3.6).

For both the AP and MM regions, there were more false detections than the 10^{-12} probability predicted. After reviewing the waveforms, it was determined that a majority of these false detections were detected by stations IMU and NMU. These stations are relatively close to the AP and MM regions. The trim window in Detex is equivalent on all stations and was too large for these closer stations. This resulted in misaligned phases on the nearby stations. These misaligned phases triggered a detection and by coincidence this occurred at the same predicted origin times for different stations.

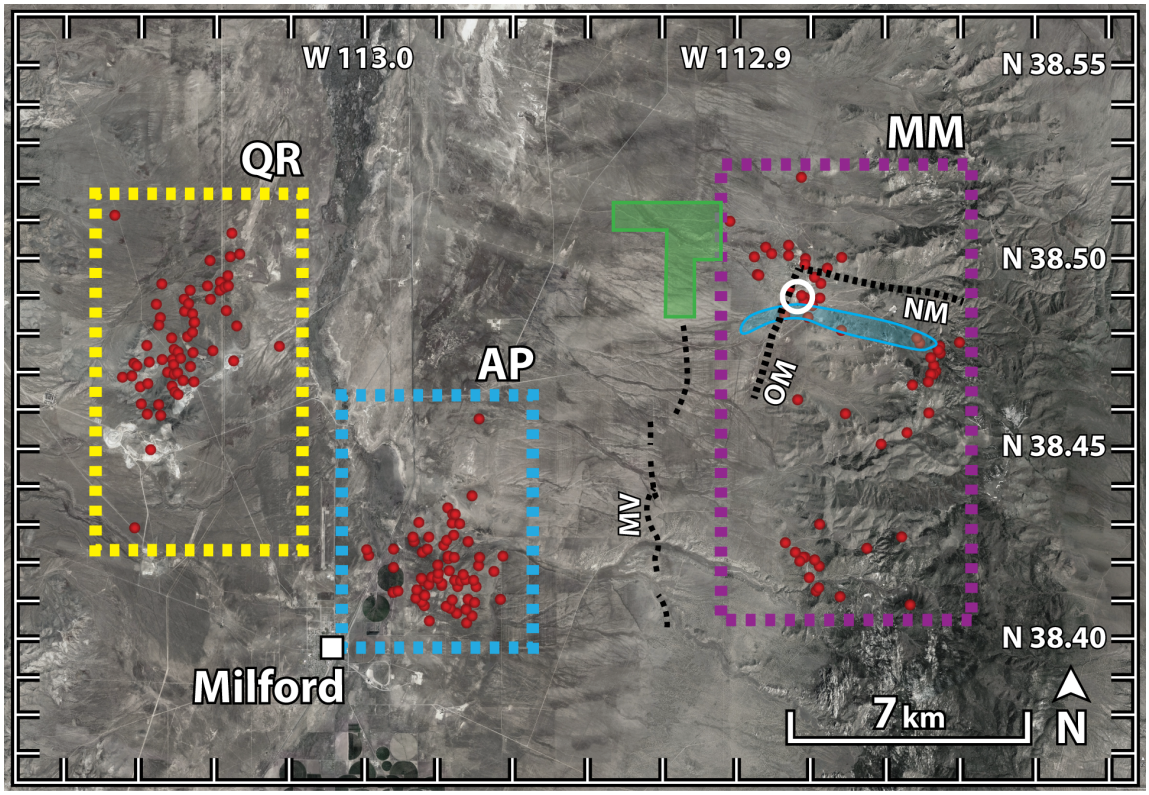

Figure 3.1. Overview of seismicity within study area 1962-2016 (red circles). Three distinct areas of seismicity present; Quarry (QR) (Yellow Box), Airport (AP) (Blue Box), and Mineral Mountains (MM) (Purple Box). White circle denotes Roosevelt Geothermal Power plant. Black dashed lines mark three major faults; Opal Mound (OP), Negro Mag (NM), and Milford Valley (MV). Green filled polygon marks the potential FORGE footprint. Blue filled shape denotes area of Zandt swarm (Zandt et al., 1982). Imagery from Google Earth.

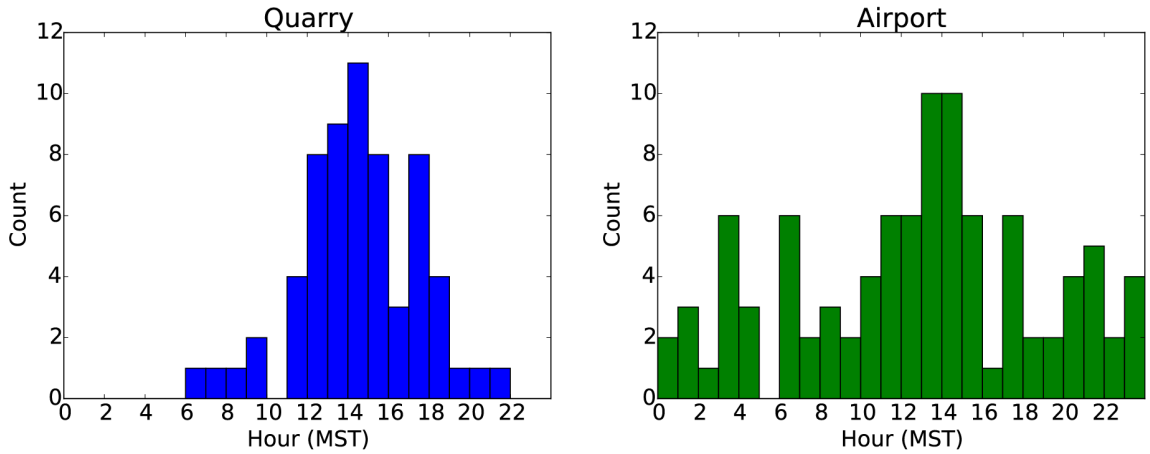

Figure 3.2. Hour versus event count diagram for Quarry and Airport. Each hour is plotted in relation to Mountain Standard Time (MST). All events from the areas denoted in Figure 3.1 are used. The Quarry shows preference for events during daylight while the Airport shows no preference.

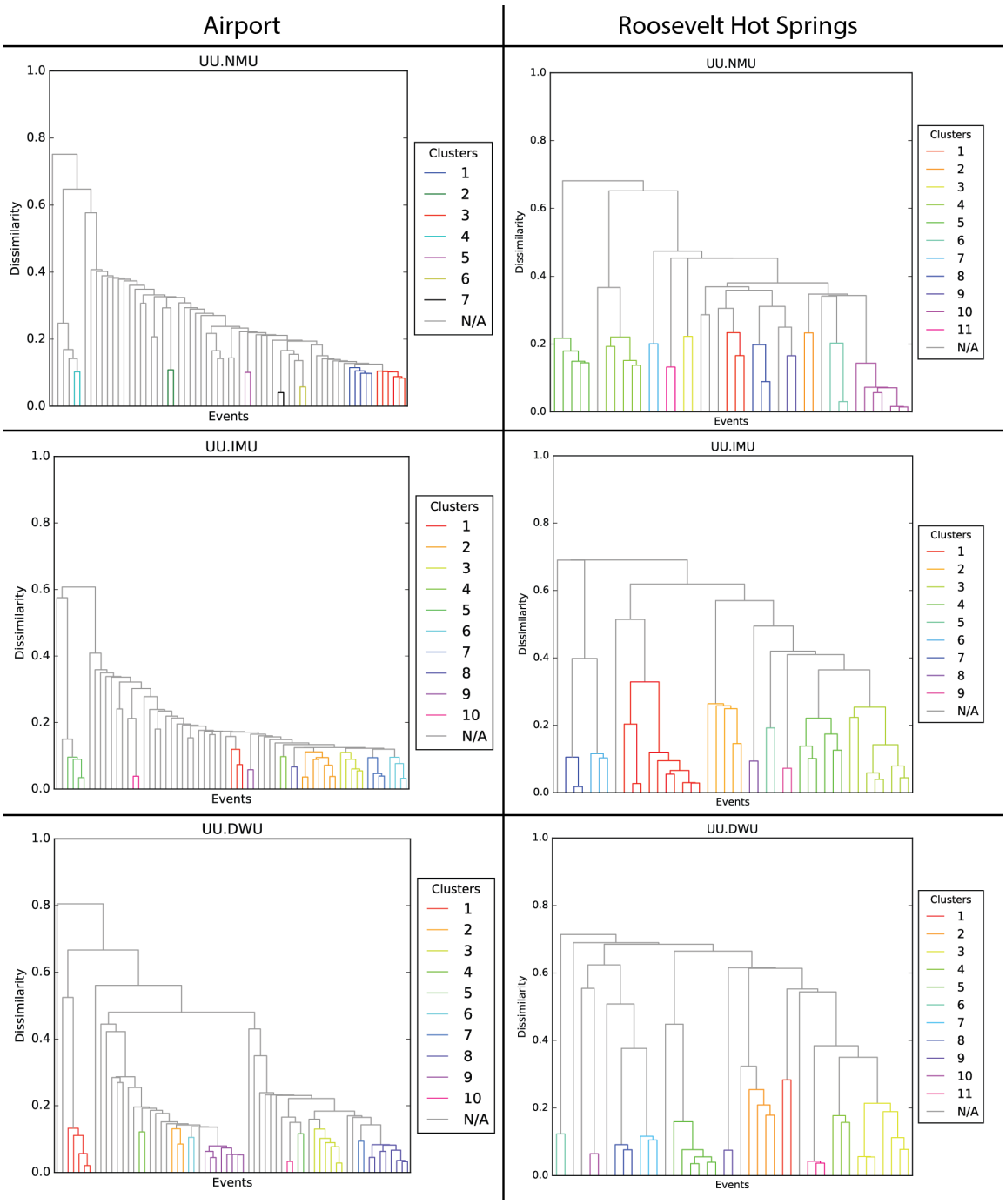

Figure 3.3. Dendrograms of the stations NMU, IMU, and DWU for the Airport (AP) and Roosevelt Hot Springs (RHS) regions. AP has few clusters and many single events. RHS is primarily composed of clusters.

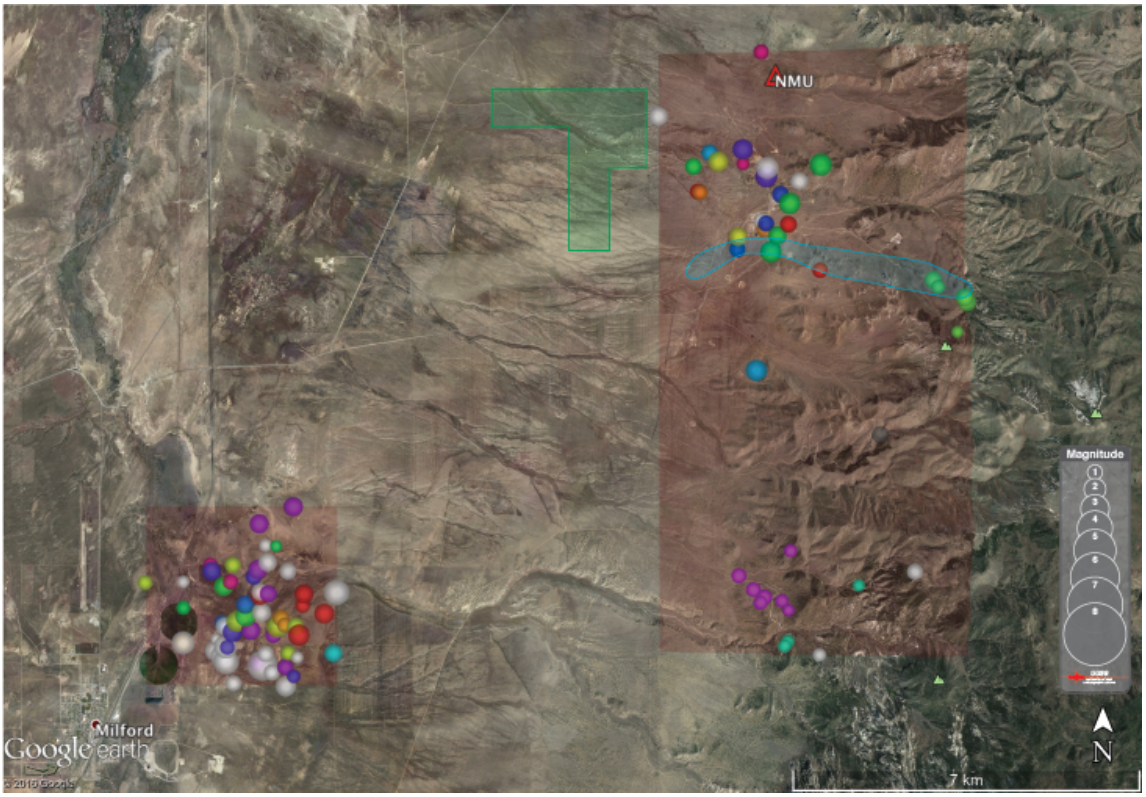

Figure 3.4. Study areas located northeast of Milford, UT from Google Earth. The seismicity ranges from 1981 to 2016. Each template event is denoted by a shaded circle. The magnitude of the event is shown by the size of the circle. The circle color denotes the cluster in which the event correlates. The larger Roosevelt Hot Springs study area in the east shows clusters using station NMU and the smaller area towards the west shows clusters using station DWU. The green polygon indicates the potential footprint for the FORGE project. The blue filled shape indicates the boundaries of the Zandt swarm (1982).

Figure 3.5. Aligned waveforms on stations NMU and basis vectors from Singular Value Decomposition for Subspace 5 (A). The difference in number is due to Detex's indexing scheme. Aligned waveforms are in no particular order. Basis vectors from singular value decomposition of aligned waveforms (B). Basis vectors ordered from greatest contribution to least based on fractional energy recovered. The blue basis vectors were chosen to represent entire subspace. Basis vector fractional energy plot. Green line indicates how many vectors are required to capture 0.9 (90%) of the fractional energy (C). Red line indicates average of fractional energy of all vectors and Grey dashed lines indicate the contribution of single basis vector.

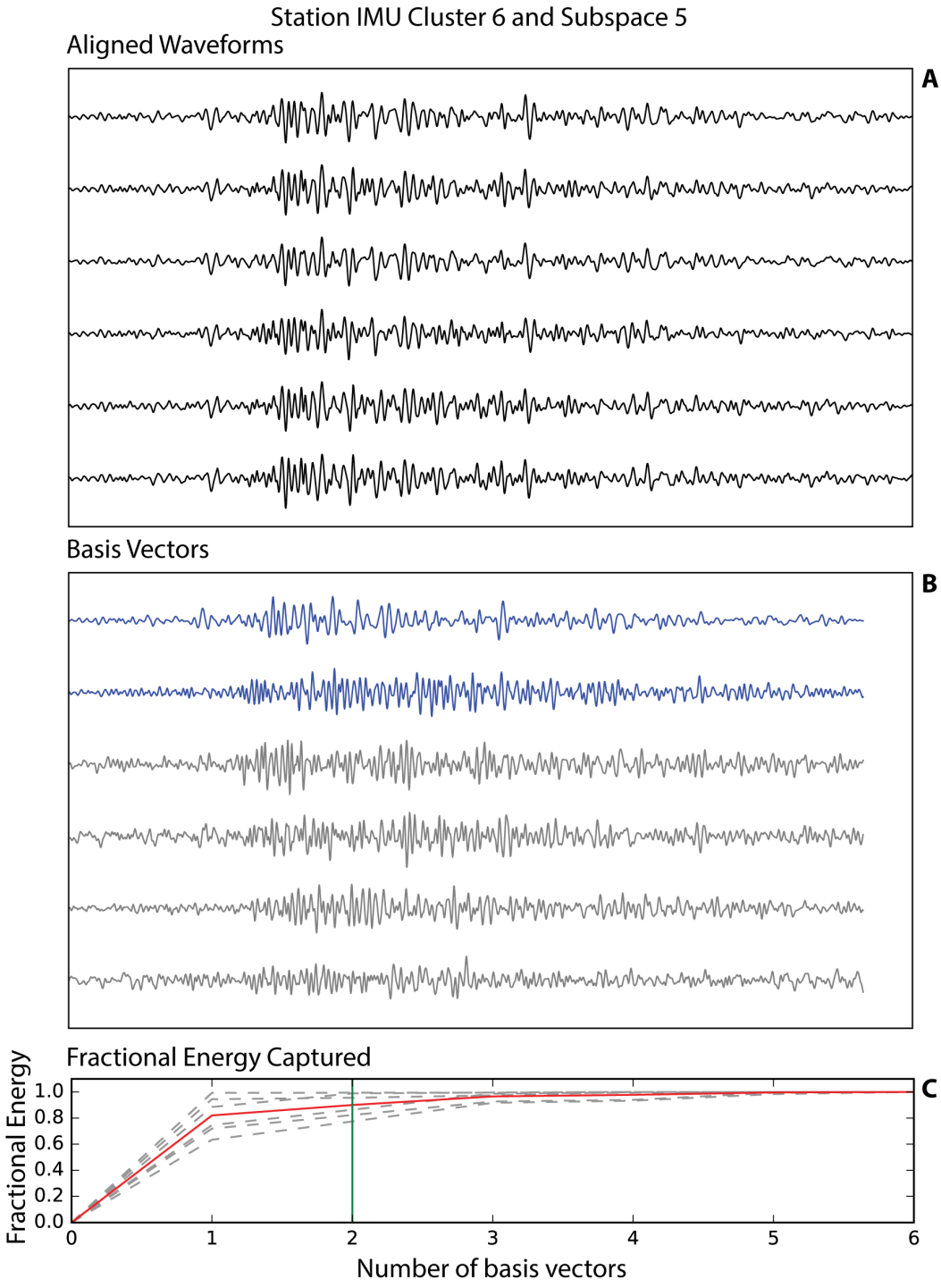
Station IMU Cluster 6 and Subspace 5
Aligned Waveforms
A
Basis Vectors
B
Fractional Energy Captured
C
Fractional Energy
1.0
0.8
0.6
0.4
0.2
0.0
0
1
2
3
4
5
6
Number of basis vectors

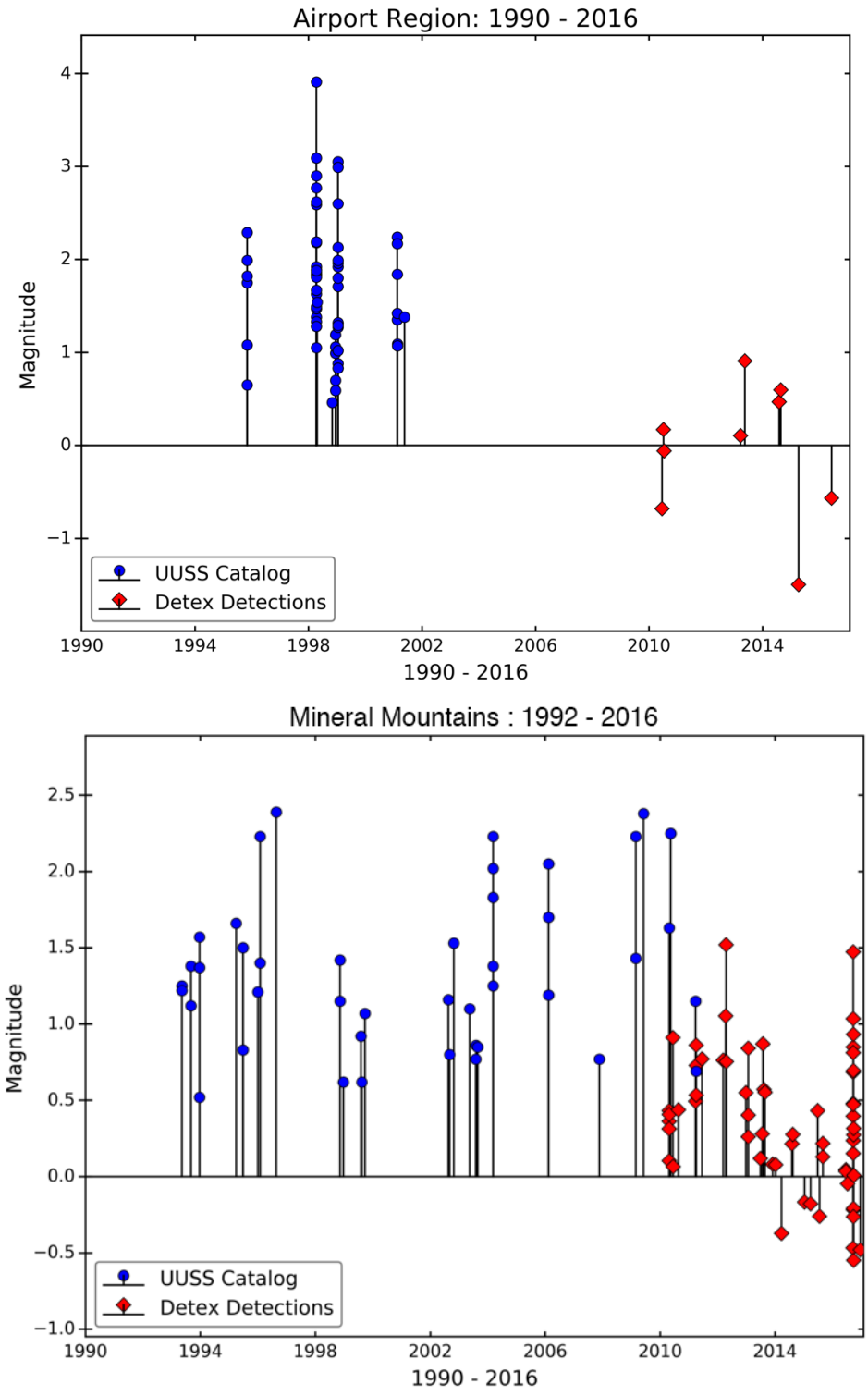

Figure 3.6. Magnitude versus time plots of Airport and Mineral Mountains areas. Blue circles represent template events and red diamonds represent manually reviewed detected events, detected from 2010-2016. The catalog extends back to 1981, but no events are in the catalog prior to 1992 and therefore, that time series is not shown.

CHAPTER 4

EARTHQUAKE LOCATIONS

To better understand the seismic sequences and their relationship to geological structures, the new detections were located together with the template events. We used GrowClust (Trugman and Shearer, 2017), a relative relocation technique that first groups all the events by waveform similarity. Similar waveforms should have similar locations and focal mechanisms (Schaff and Waldhauser, 2005). Each similar group or cluster is then located using cross-correlation lag times. These multiple clusters are located in the same reference frame.

A benefit of using GrowClust is that errors are reported based on bootstrap resampling. In bootstrap resampling, a random resampling vector is generated and the resampled cross-correlation data are then rerun through the location algorithms. This produces a set of locations that are perturbed from the original location. Based on the number of bootstrap iterations, a distribution of hypocenters is attained. Errors in GrowClust are nonparametric error estimates obtained from the Median Absolute Deviations (MAD), equation 4.1, of the hypocentral locations bootstrap distribution (Leys et al., 2013; Trugman and Shearer, 2017),

$$MAD(X) = median(|X_i - median(X)|) \quad (4.1)$$

where X_i is the hypocentral location for an event and X is the hypocentral location of all the events within the data set.

4.1 Data

All events used in GrowClust require an origin time and initial location. Origin times were determined through Detex from the template events that triggered the detection. Subspace detection, however, does not produce locations. While using a centroid is feasible, it is not optimal given the geographic extent of the study area, where events locate from north to south across several kilometers, and the multiple waveform clusters, especially in the Mineral Mountains (MM). If the centroid were chosen as a starting location for all new detections, then the relocation of the events would be more influenced by the centroid then by the waveform family.

Initial locations for the detected events were derived based on their correlation with the template events. In order to gain a starting location for the newly detected events, all template and detected events were cross-correlated. Then the detected event with the highest cross-correlation value to a template event was given the template event location. The starting location for some of the detected events shifted depending on which station was selected to compare detected-template cross-correlation values. To limit such variations, we use the cross-correlation results from station NMU. All template event locations were from the UUSS earthquake catalog. For the template events, all available stations used in the initial catalog location were used in the relocation. These

stations are UUSS network stations: PSUT, TCRU, IMU, NMU, DWU, MSU, and MVU. Not all events were observed on all stations. For these stations, waveforms from all events were cross-correlated at common stations to get lag times. Because the largest amplitude energy in the cross-correlation window is the S-phase, the lag time is associated with differences in S-arrival times. For the newly detected events, only stations NMU, IMU, and DWU were used to determine lag times, due to the small magnitude of the events. The Python software package was used to convert the Detex output files into files ready for use in GrowClust.

4.2 Relocation

For calculating locations in both the AP and MM regions, the same basic parameters were chosen and prescribed. Travel time tables for P- and S-waves were calculated for depths 0-26 km in 1 km increments and distances of 0-200 km in 2 km increments. The velocity model used in these calculations was the Trail Mountain velocity model (Figure 4.1) (Pechmann et al., 2002). The minimum cross-correlation coefficient required to compute an event-pair similarity coefficient was 0.02. Maximum station distance used in the calculation for event-pair similarity coefficient was 80 km. The maximum root-mean-square differential residual for a proposed cluster merger was 0.2 during relocation. I kept all the differential time observations throughout relocation but only allowed events to relocate for similarity coefficients above 0.02. Minimum number of events in a cluster branch was 1. The number of bootstrap iterations tested was 10, 40, and 100. The final event hypocenters did not change through any of the bootstrapping runs, but the errors did shift slightly. Median horizontal error was 0.194

km, 0.174 km, and 0.169 km for 10, 40, and 100 bootstrap iterations, respectively. Median depth errors were 0.116 km, 0.110 km, and 0.117 km for 10, 40, and 100 bootstrap iterations, respectively. The weighting of all the events were equal. Locations reported come from the initial locations derived from cross-correlation results from station NMU and 100 bootstrap iterations.

4.3 Results

Of the 74 total events for the Airport (AP), 52 template events and 4 detected events were relocated (Figure 4.2). Initial locations for the template events came from the original UUSS catalog. Those events that did not relocate remained at their initial locations. Events that did not relocate did not cluster with any other event (e.g., waveforms too dissimilar); 13 template events and 5 detections were not relocated. The depths for the relocated events range from 0.05 km to 9.07 km depth. The relative median error in depth and horizontal position is 0.56 km and 0.19 km, respectively.

For MM, 36 template events and 41 detected events were relocated of the total 104 earthquakes (Figure 4.3); 7 template events and 20 detected events were not relocated. Those nonrelocated events remained at their initial locations. Depths ranged from -0.03 km to 7.28 km with a median error of 0.117 km. Median horizontal error is 0.169 km. While GrowClust is a relative relocation program, the results show that the absolute locations agree well with past seismicity and the recorded locations of the Zandt swarm (Figure 4.4).

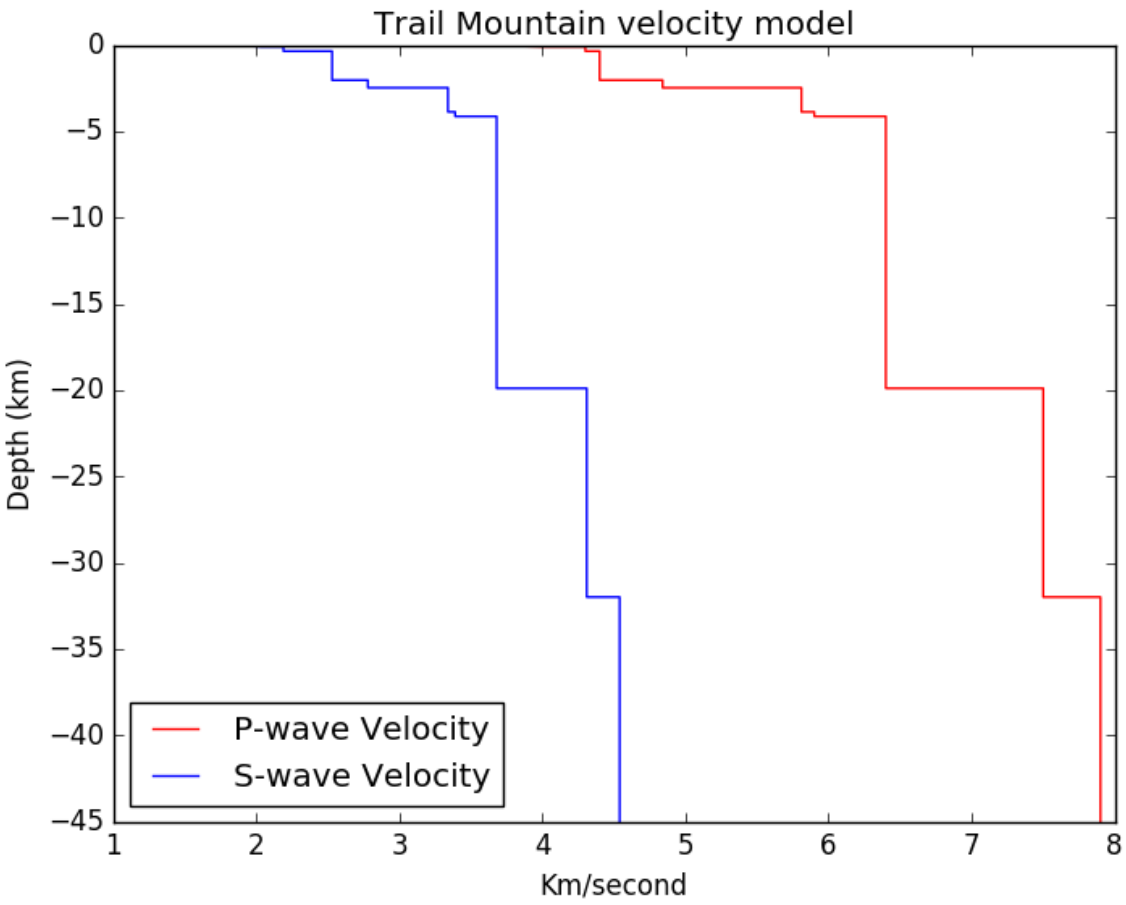

Figure 4.1. Velocity model used in the relocation process with GrowClust. The Trail Mountain velocity model has been calibrated with sonic logs in the shallow crust.

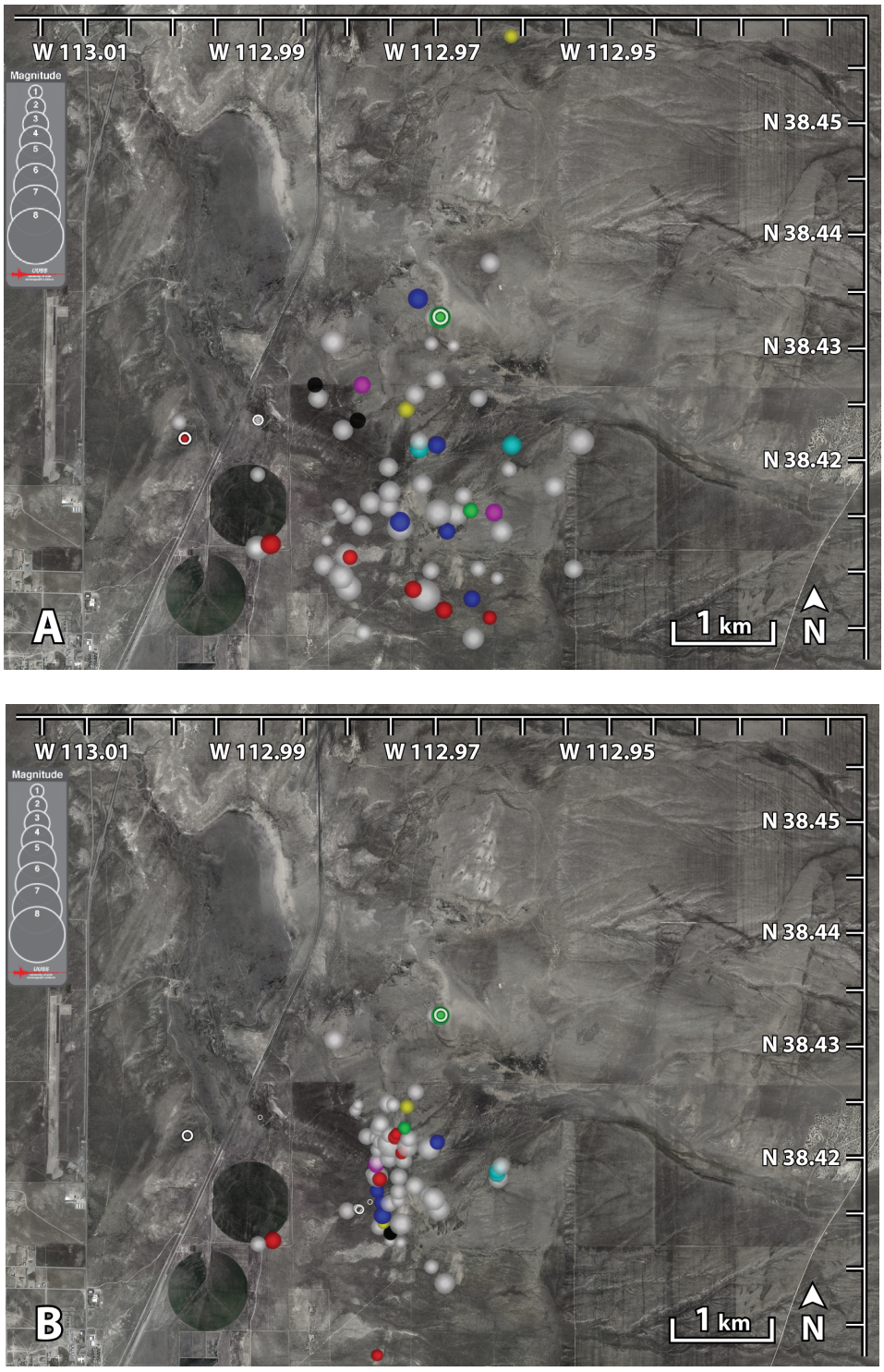

Figure 4.2. Pre (A) and Post (B) relocation of events at Airport. Colors denote the cluster in which they belong from NMU, white color denotes singleton. Solid circles are template events and open circles are detected events.

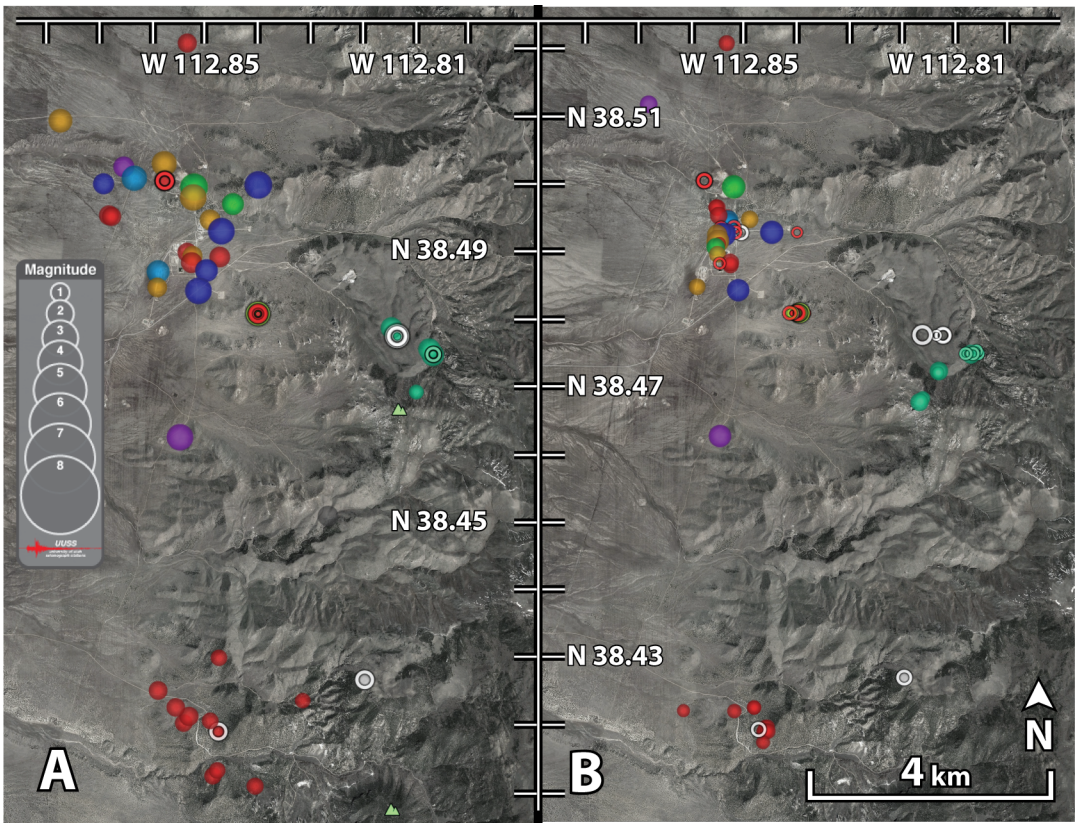

Figure 4.3. Pre (A) and Post (B) relocation of events in Mineral Mountains. Colors denote the cluster in which they belong from NMU, white color denotes singleton. Solid circles are template events and open circles are detected events.

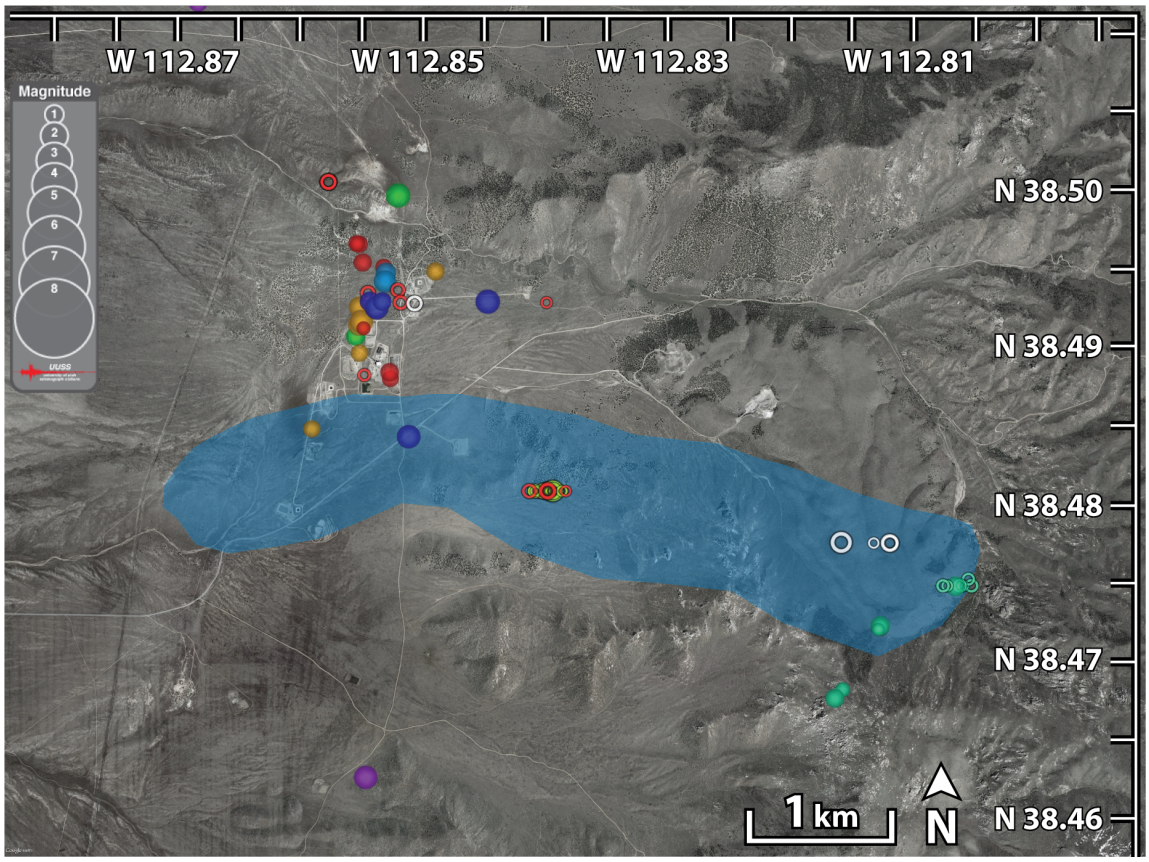

Figure 4.4. Relocated events in relation to Zandt swarm (blue filled outline). Relocated templates (solid circles) and detected events (open circles). Color denotes cluster from station NMU, and white denotes singleton. Seismicity just north of Zandt swarm zone is located around the Roosevelt Hot Springs geothermal system.

CHAPTER 5

FAULT GEOMETRY

With all events being relocated relatively, the geometry of the seismicity for the areas of interest can be observed visually with a 3D projection from various angles. Visual inspection is qualitative and a more quantitative approach in determining the geometric pattern is important. Principal Component Analysis (PCA) has been previously used to determine hypocenter geometries (Michelini and Bolt, 1986; Shearer et al., 2003; Gammans, 2013). This statistical method quantifies the spread of the data, hypocenters in this case. PCA can indicate whether the hypocenters cluster around a line, plane, or a sphere. In this case, the data are in an *xyz* coordinate system. As such, three orthogonal axes are oriented from the direction of maximum to minimum spreading, or variance.

An Eigen-decomposition on the covariance matrix of hypocenter data is necessary to complete a PCA. The subsequent eigenvectors define the orientations of the principal axes. The eigenvalues describe the magnitude of each of the axes. The covariance matrix (V) is 3 x 3 and can be found using equation (5.1) for x_1, x_2, and x_3

$$V_{ij} = \frac{1}{m}\sum_{k=1}^{m}\left(x_i^k - \bar{x}_i\right)\left(x_j^k - \bar{x}_j\right) \qquad i,j = 1,2,3 \tag{5.1}$$

where m is the number of events, x is the event location, and $\bar{x}$ is the mean of the location with i and j and representing *xyz* locations. λ_1, λ_2, and λ_3 are the resulting

eigenvalues where $\lambda_1 > \lambda_2 > \lambda_3$. U_1, U_2, and U_3 are the corresponding eigenvectors.

The events have a nearly spherical distribution pattern when $\lambda_1 \approx \lambda_2 \approx \lambda_3$. Those hypocenters that define a line have $\lambda_2, \lambda_3 \ll \lambda_1$ and cluster around a single axis. Hypocenters define a plane if $\lambda_2/\lambda_3 \geq 8$ (Shearer et al., 2003) and the standard error of the plane's orientation does not exceed 20° from bootstrap resampling (Shearer et al., 2003).

Planarity of the hypocenter distribution can also be quantified using equation (5.2)

$$planarity = 1 - \frac{2\lambda_3}{\lambda_1 + \lambda_2} \tag{5.2}$$

where a planarity of 1 is completely planar and 0 is spherical. Linearity of the clustering may be quantified using equation (5.3)

$$linearity = 1 - \frac{\lambda_2 + \lambda_3}{2\lambda_1} \tag{5.3}$$

where 1 defines a completely linear spread. The eigenvalues describe the magnitudes of the axes and by taking the square root of each eigenvalue the radial length of the axis is given. Multiplying the radial length by 2 yields the axis length.

5.1 Airport

First, a visual inspection of Airport (AP) seismicity was conducted. A potential plane was visible in the qualitative analysis with a small outlier group with longitudes west of -112.965° (Figure 5.1). Only events that were successfully relocated were used in the analysis. Fifty-one events were used in the analysis and yielded $\lambda_1 = 5.88$, $\lambda_2 = 0.24$, and $\lambda_3 = 0.013$. Since $\lambda_2/\lambda_3 \geq 8$, the solution of the distribution of the AP is

along a plane, with planarity = 0.996 (Figure 5.1). The plane dips towards the east with a length, L, of 4850 meters and a minor axis with a width, W, of 985 meters. The length of the plane is approximately 500% the width.

The normal to the plane is the direction with the smallest variance, so by taking the inverse of equation 5.4 (Stein and Wysession, 2003), the strike and dip of the plane can be estimated in the initial coordinate system

$$\hat{n} = \begin{bmatrix} -sin\delta sin\theta \\ -sin\delta cos\theta \\ cos\theta \end{bmatrix} \tag{5.4}$$

where δ is the dip angle and θ is the strike azimuth. Using the third eigenvector from the primary seismicity cluster as the normal, the strike of the seismicity is 176.4° and the dip is 89.9° toward the east.

In order to test the stability of the PCA calculations, a jackknife approach was used where a single event is removed from the dataset and then PCA is recalculated. The event is then returned to the dataset and another event is removed and this iterative process is repeated through the entire dataset. The jackknife results in the AP event's strike and dip errors of 0.99° and 0.15°, respectively, at 1σ confidence interval. The hypocenter distribution for planarity was calculated to be 0.996 ± 0.0002. These results indicate that there were no significant outliers and it appears that the geometry was stable throughout the jackknife analysis. The outlier group of events was also analyzed and failed to produce a stable PCA.

5.2 Mineral Mountains

PCA was also applied to the Mineral Mountain (MM) region, with a focus on the events that fall in the Zandt swarm area (Figure 5.2). There are a total of 41 template and detected events that relocated into and near the Zandt swarm region. After PCA, $\lambda_1 = 11.73$, $\lambda_2 = 0.0497$, and $\lambda_3 = 0.0047$. As $\lambda_2/\lambda_3 > 8$, the events cluster along a plane with planarity = 0.999. The length (L) of the plane was 6.85 km with a width of 0.45 km. The strike of this plane is 22.4° dipping 87.6° towards the east.

The stability of the PCA calculation was tested, with a jackknife approach identical to the AP region, for the final locations for the Zandt swarm region. The jackknife results in strike and dip errors of 11.67° and 45.63°, respectively, at 1σ confidence interval. Planarity for the seismicity cluster was calculated to be 0.9992 ± 0.00004. The results of the jackknife analysis show that the plane solution is unstable.

The region on the southern end of the MM study region was also separated visually (Figure 5.3) and PCA applied to these events. Ten events produced $\lambda_1 = 0.804$, $\lambda_2 = 0.014$, and $\lambda_3 = 0.0006$. The planarity of the cluster of events was 0.998. The length (L) of the plane was 1.79 km with a width of 0.24 km. The strike and dip of the plane were 167.98° and 81.52° east, respectively. The standard deviation within 1σ from bootstrapping was 7.30° for the strike and 49.42° for the dip. Error for the planarity of the solution was 0.001. Resulting jackknife errors show that the planar solution for the southern Mineral Mountains is unstable.

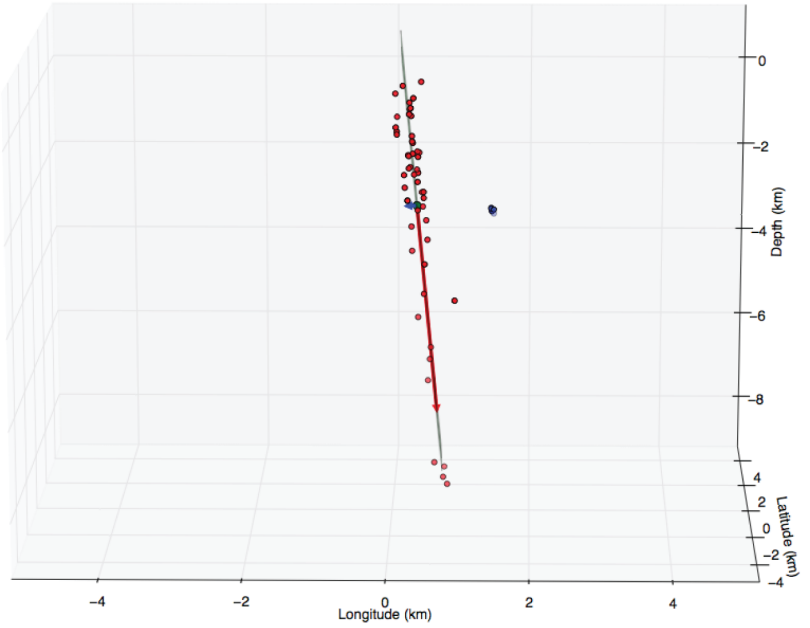

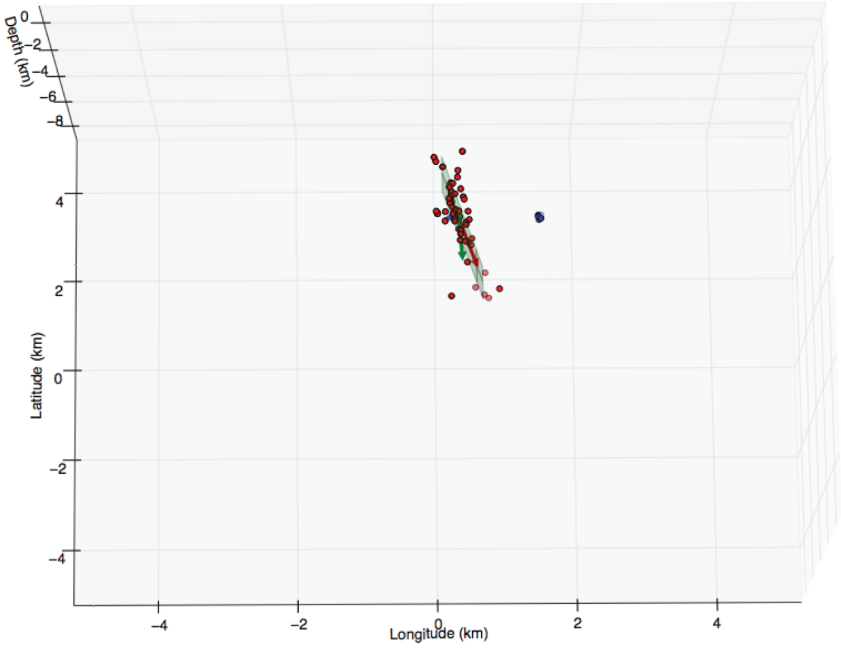

Figure 5.1. Planar PCA results for Airport from the events in red. Those events in blue were not used in the calculation. The Eigen vectors are plotted 1 (red), 2, (green), and 3 (blue). Green plane for visualization of directions. Latitude and longitude are plotted based from a reference frame of all points minus their mean positions.

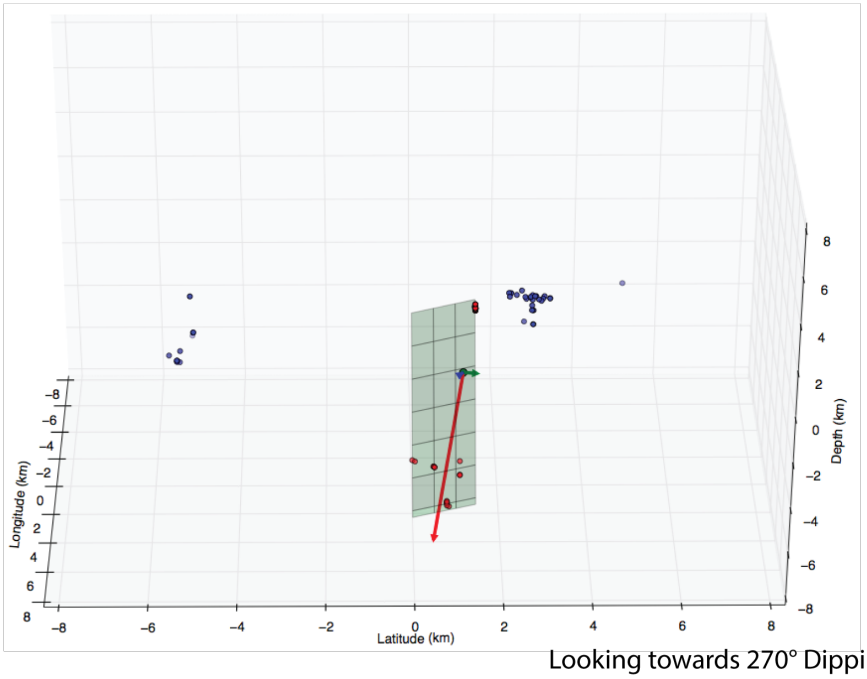

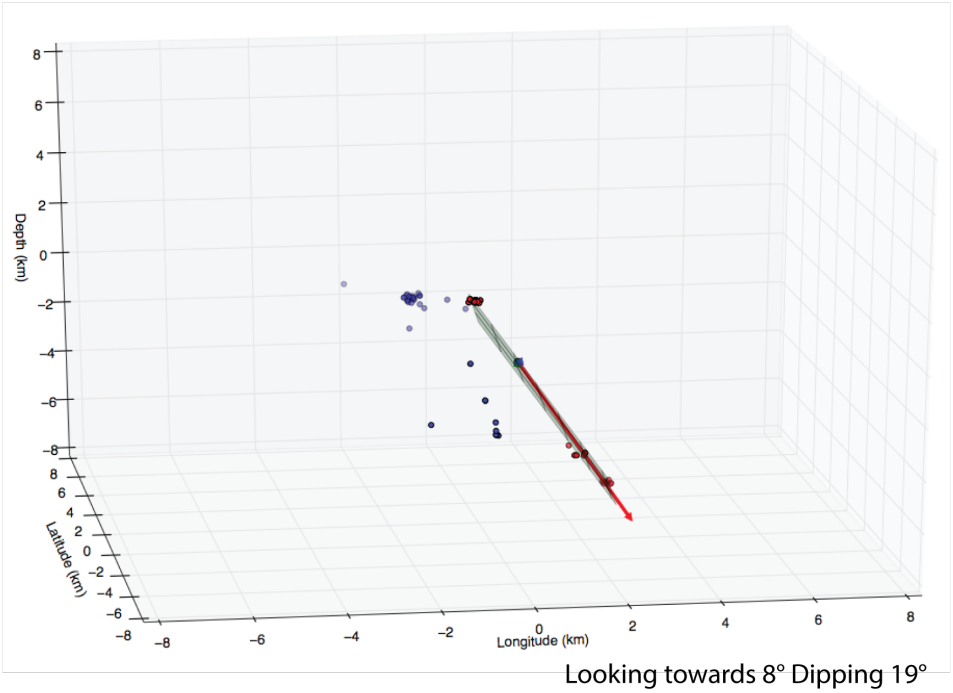

Figure 5.2. Linear PCA result for Mineral Mountains, swarm area, from the events in red. Those events in blue were not used in the calculation. Latitude and longitude are plotted based from a reference frame of all points minus their mean positions.

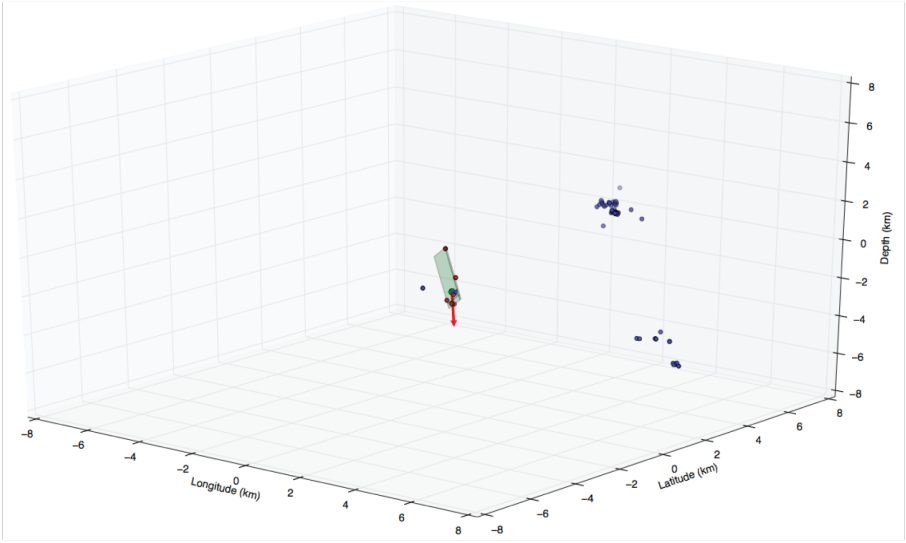

Looking towards 310° Dipping 22°

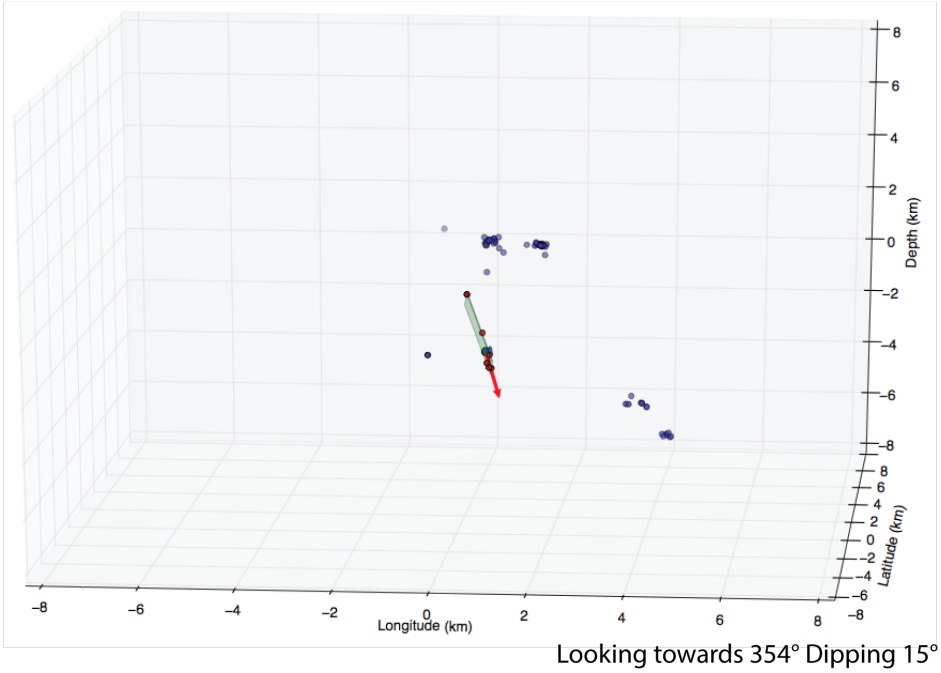

Looking towards 354° Dipping 15°

Figure 5.3. Planar PCA results for Mineral Mountains, southern area grouping, from the events in red. Those events in blue were not used in the calculation. The Eigen vectors are plotted 1 (red), 2, (green), and 3 (blue). Green plane for visualization of directions. Latitude and longitude are plotted based from a reference frame of all points minus their mean positions.

CHAPTER 6

RESULTS AND DISCUSSION

The results of the noise analysis have shown that while high background noise is persistent during a few time ranges within the period of study, making microseismic event detections challenging, a majority of the data from 1 Hz to 10 Hz nevertheless has low noise. This observation supports our ability to detect microseismic events in these frequencies. Although using direct waveform analysis was not completed in this study, Harris (2006) explored the benefits of subspace over matched filters; he found that noise analysis and subspace detections were important steps in being able to confidently lower the magnitude of completeness for a given area of study.

With the confirmed detected events added to the seismic catalog in the Milford Valley region, I recalculated the magnitude of completeness (M_{comp}). A robustly determined and lowered M_{comp} for the FORGE site is an important step in designing the induced seismicity mitigation plan for the geothermal experiment. A qualitative assessment of the number of events for a given bin count shows that the M_{comp} before and after the detections are added to the catalog is 1.75 and 1.0, respectively (Figure 6.1). A quantitative review of the stability of the b-value can help determine if the observed M_{comp} is acceptable (Figure 6.1). We calculate this stability by taking the maximum likelihood estimation of the b-value for an assumed M_{comp}. If an incremental change to

the M_{comp} results in a change in b-value less than 0.05, I consider the result to be stable. For the catalog prior to the added detections, the stable b-value is 0.82 ± 0.14 with an M_{comp} of 2.0, which is higher than previously reported 1.7 (Pankow et al., 2004). With the added detections, the stable b-value is 0.68 ± 0.07 with an M_{comp} of 1.5. To visualize this, a cumulative magnitude plot for both catalog events and catalog plus detection events was compiled (Figure 6.2) and binned in 0.25 magnitude units. For these source regions, M_{comp} was reduced from 2.0 to 1.5, according to a stable b-value result. A b-value less than one supports the observed low seismicity in the area.

Seismicity was located in three distinct areas of the Mineral Mountains (MM) region; (1) the area surrounding the Roosevelt Hot Springs geothermal plant (RGP), (2) an area toward the south near the central MM, and (3) the Zandt swarm zone (Figure 6.3). There is concern for induced seismicity around the RGP because pumping fluids at depth for geothermal systems has induced seismic events at other geothermal facilities (e.g., Deichmann and Giardini, 2009; Terakawa et al., 2012; Mukuhira et al., 2013; Grünthal, 2014; Zang et al., 2014). Although some geothermal plant operations are associated with induced seismicity, we suggest the risk at RGP may be low: the pumping history of the RGP with the seismicity in the MM does not yield a clear correlation (Figure 6.4). Zandt et al. (1982) reached a similar conclusion based on the original test wells. Seismic events do locate under RPG, and these events occur at shallow depths from 0.04 km to 1.57 km. We cannot rule out the the possibility that these events are induced, and note that without an observable increase in events correlated with fluid injection, as seen in other fluid injection studies (e.g., Evans et al., 2012; Deichmann et al., 2014; Grünthal, 2014; Zang et al., 2014), discriminating them from natural events remains challenging.

The seismicity that has been observed along the southern edge of the study area for the MM region has events at depths between ~0.5 km and ~5 km. By completing a principal component analysis (PCA), it was found that the solution was unstable due to the few available events. Through visual observations, the general trend of the events is consistent with mapped north-south structures (Nielson et al., 1978, 1986; Sibbett and Nielson, 1980).

There are 41 events, both from the catalog and new detections, in the swarm zone originally identified by Zandt et al. (1982) (Figure 6.3). Applying PCA to the data from the Zandt swarm zone resolves a planar feature ($\lambda_1 = 11.73,\ \lambda_2 = 0.0497,$ and $\lambda_3 = 0.0047$) with planarity = 0.999. The strike and the dip of the plane is 22.4° and 87.6° toward the east, respectively, and is consistent with reported north-south structures in the Mineral Mountains such as the Opal Mound fault (e.g., Sibbett and Nielson, 1980; Zandt et al., 1982). The events found in the Zandt swarm zone relocated by our analysis separated into two distinct depth zones, one between 5.75 km and 7.28 km depth and the other approximately from the surface to 0.14 km depth. This is consistent with the observation made by Faulder (1991) regarding a seismicity gap in depth, although the gap reported by Faulder was between 3.05 km and 7.92 km, whereas the relocated events in this study indicate a gap between 0.14 km and 5.75 km. Although the depths may differ, the magnitude of the gap in seismicity differs by less than 1 km. The difference in reported depths may result from different data frames (e.g., sea level datum) and processing algorithms.

Fifteen of the 41 events in the Zandt swarm zone occurred between September 21 and September 22, 2016 and ranged in magnitude from M -0.26 to M 1.47. Since there is

no clear main-shock within the sequence, I refer to this sequence as a swarm. All events in the swarm were detected from the subspace analysis and were located in the middle of the Zandt swarm zone. The depths were shallow, ranging from -0.03 km to 0.124 km. The events migrate away from the first event consistent in time and space with fluid migration (Figure 6.5; Hainzl, 2004; Shelly et al., 2013). I interpret these events to be related to fluid propagation. More events may be occurring within the swarm zone to better support this, but are below the magnitude threshold of detectable events.

For the Airport (AP) region, PCA of the distribution of events shows that the seismicity is best fit by a plane. This plane has no mapped surface expression. Additional seismic and geomorphic analysis is needed to confirm the existence of this fault. A possible potential surface geometry is shown in Figure 6.6. While the potential AP fault plane strikes at 176.4° and dips 89.9° east, there is a small outlier group that lies just east of the plane. It is unclear how the outlier group of events and the main plane are related. The larger cluster that defines the plane is consistent with the geometry described by the moment tensor for the April 10, 1998 M_L 3.91 event (Figure 6.6) (Whidden and Pankow, 2012).

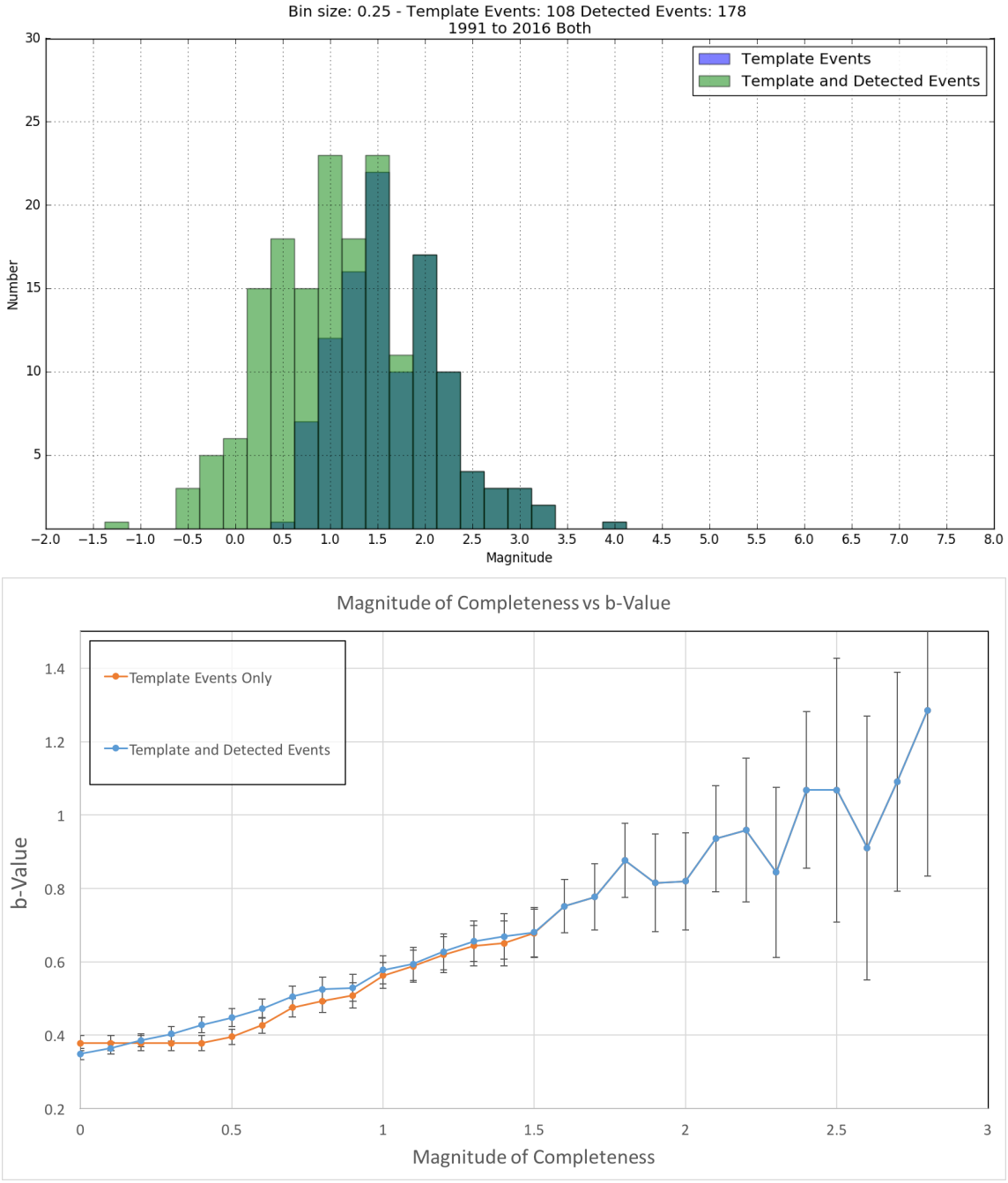

Figure 6.1. Magnitude versus event count histogram of template and detected events for both the Airport and Mineral Mountains. Top figure represents the event count per bin for template events only (blue) and template and detected events (green). Bin size is 0.25. Bottom figure represents assumed magnitudes of completeness versus b-value. Low seismicity in the area is supported by the low b-values presented. Template and template with detected event lines begin to overlap at magnitude of completeness 1.5 and above.

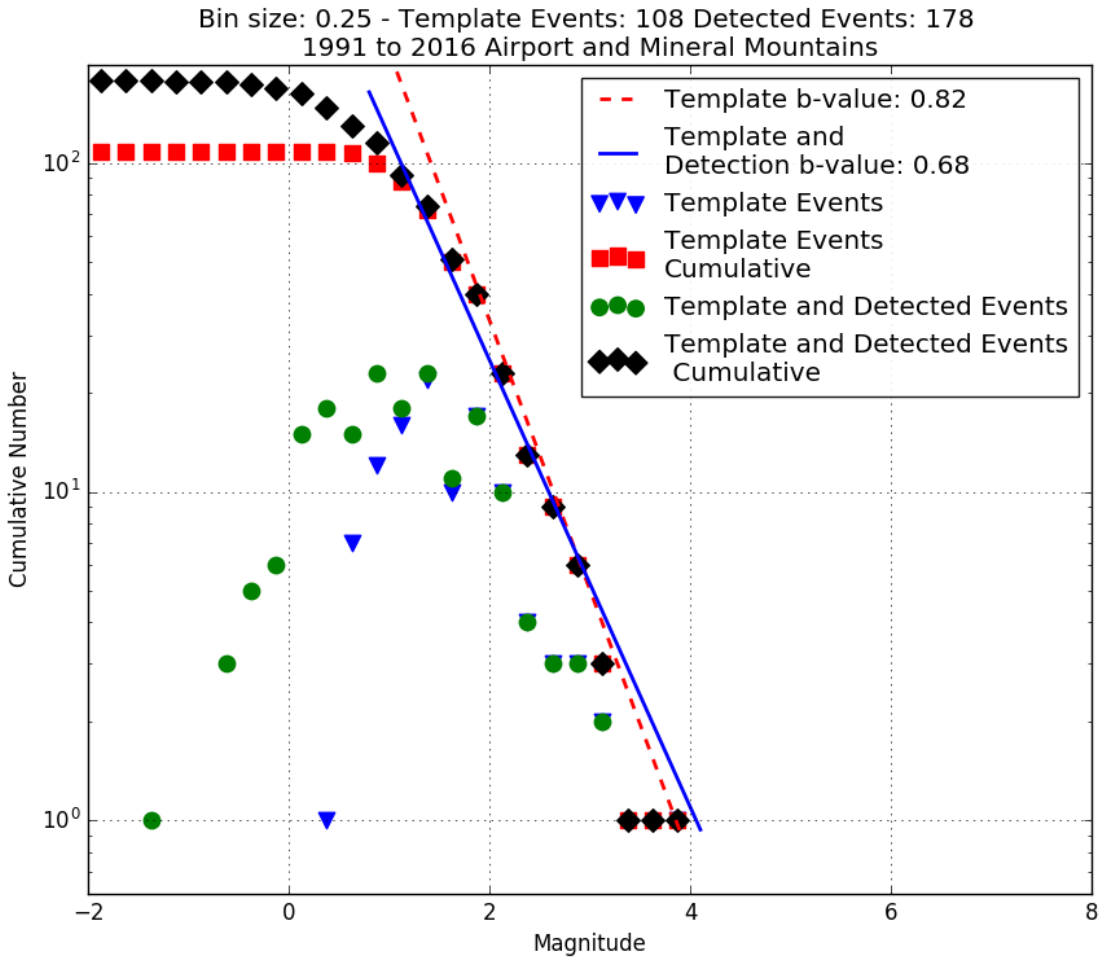

Figure 6.2. Magnitude versus event count of template and detected events for both the Airport and Mineral Mountains. Figure shows individual bin counts (blue inverted triangles = template events only, green circles = template and detected events) and cumulative magnitude counts (red squares = template events only, black diamonds = template and detected events). Blue solid line is b-value of template events with detections. Red dashed line is b-value of template events only. Bin size for figure is 0.25.

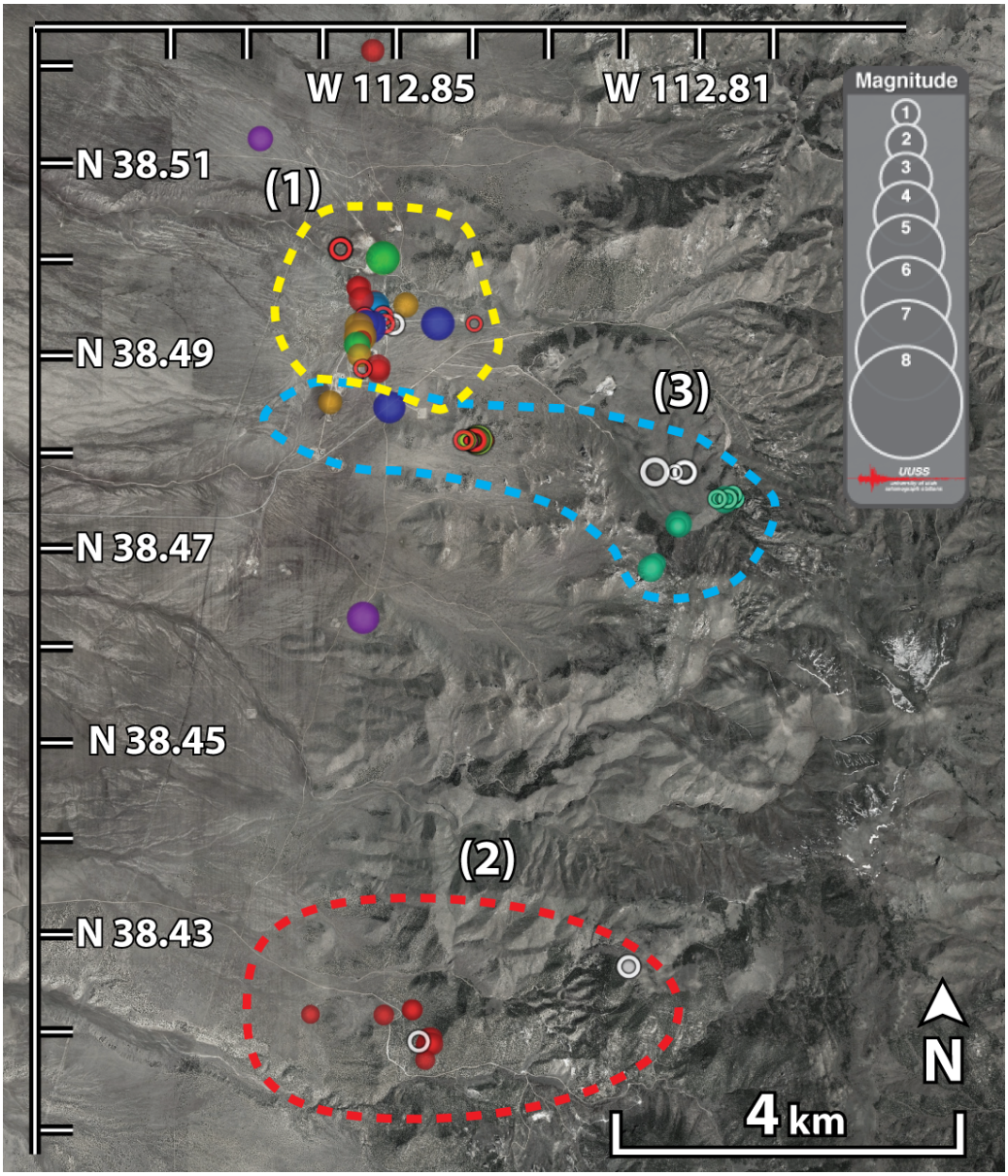

Figure 6.3. Three distinct areas of seismicity seen in the Mineral Mountains: (1) under the Roosevelt Hot Springs System, (2) south of the study area in the central Mineral Mountains, and (3) the seismicity that occurs within the Zandt swarm zone.

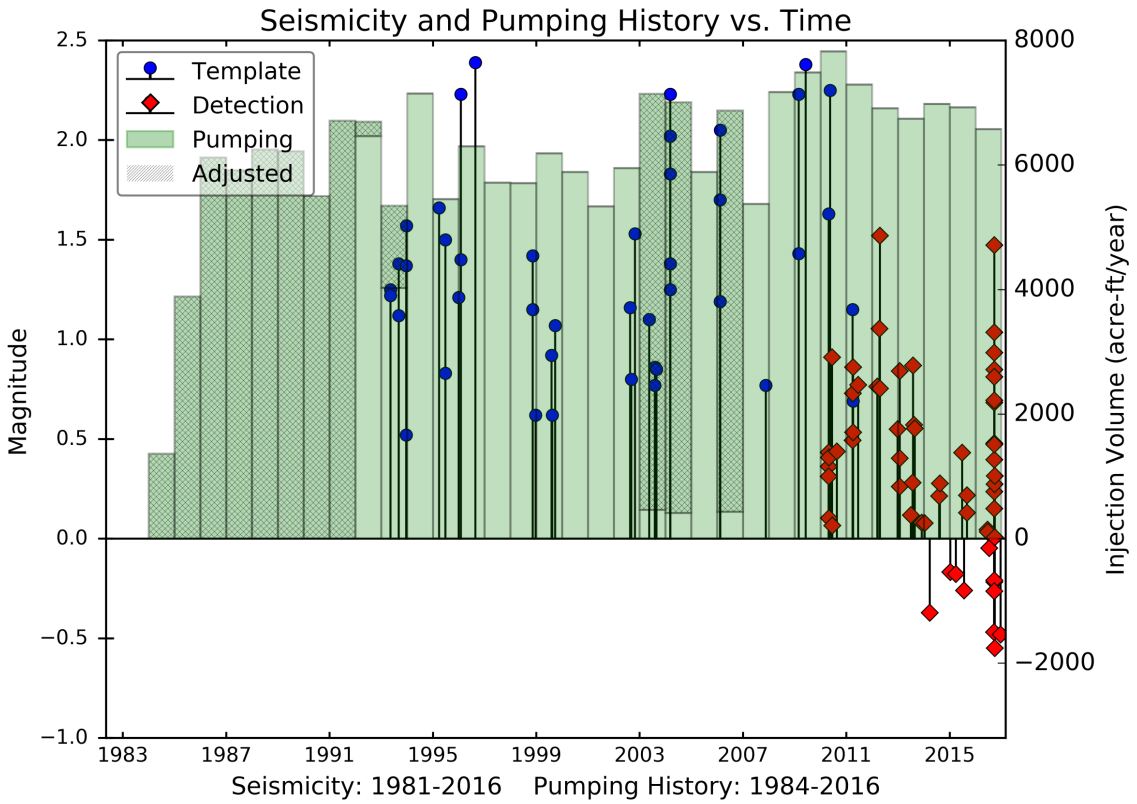

Figure 6.4. Seismicity versus pumping history of the Roosevelt Hot Springs geothermal plant, including subspace detected events (red diamonds) and template events (blue circles) in detection work. The pumping history (green bars) is shown for each quarter from 1981 through 2016. The pumping history comes from the published data from waterrights.utah.gov. The adjusted pumping history, with hash marks, comes from the need to correct the data found on waterrights.utah.gov. This correction was completed based on the reported power produced and discrepancies in the reported fluid production. Original template events occur from 1993-2011.

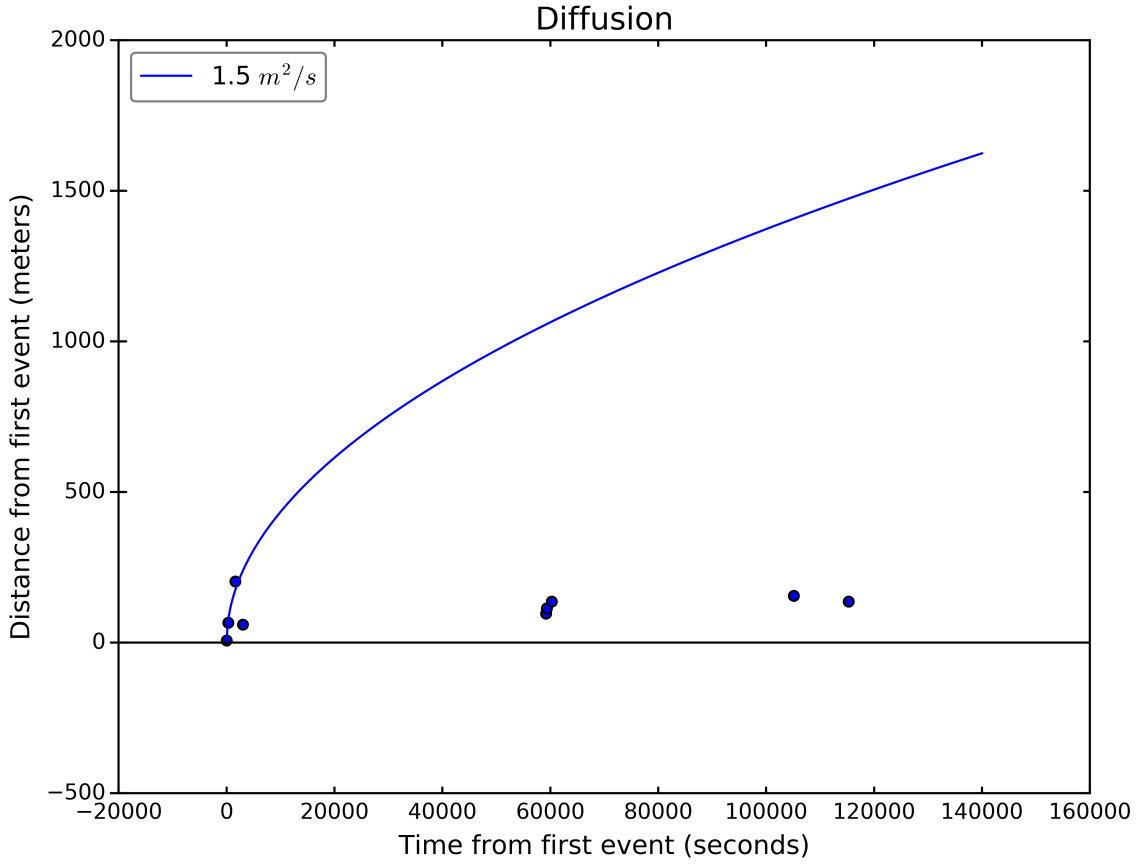

Figure 6.5. Diffusion plot for swarm events (September 21-September 22, 2016). All events (blue circles) are plotted relative to hypocentral distance from first event. Distribution of events relative to the first event that occurred in sequence. Blue line represents diffusion rate (1.5 $\frac{m^2}{s}$) using $r = \sqrt{4\pi Dt}$ where r = radius from first event, D = diffusion rate ($\frac{m^2}{s}$), and t = time from Shelly et al. (2013).

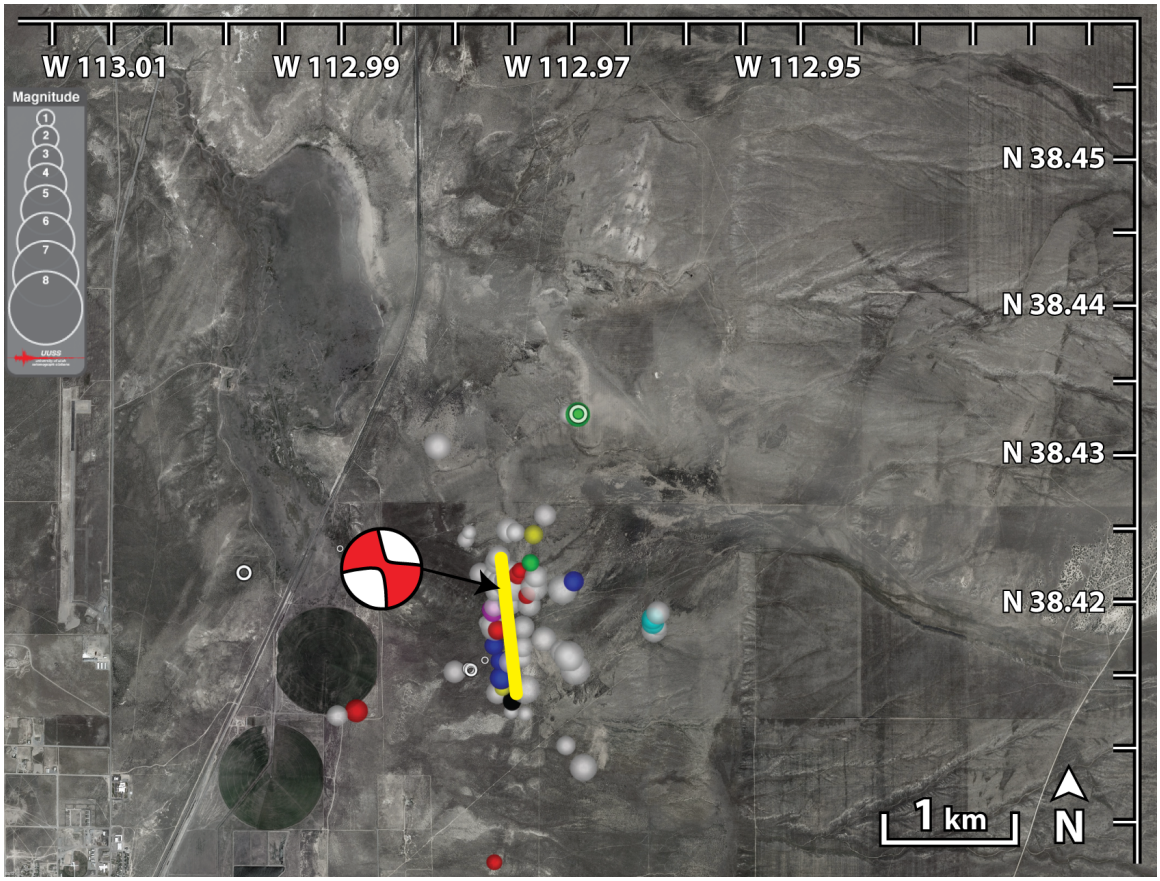

Figure 6.6. Relocated Airport events with planar strike. Colors denote the cluster in which they belong from NMU, white color denotes singleton. Solid circles are template events and open circles are detected events. Yellow line is the strike of the PCA solution and matches closely with the moment tensor solution for the April 10, 1998 M 3.9 event (Whidden and Pankow, 2012).

CHAPTER 7

CONCLUSION

The analysis described above has added 43 new events to the seismic catalog for 2010 – 2016, bringing the total number events for this area to 178. The seismicity within Milford Valley occurs largely in two distinct regions: the Airport (AP) and the Mineral Mountains (MM). The AP seismicity suggests a plane that has a strike and dip consistent with a previous focal mechanism near the site (Whidden and Pankow, 2012). The MM region has three sub-areas of seismicity: the Roosevelt Hot Springs geothermal power plant, the southern area, and the area identified as the Zandt swarm zone. The seismicity in the Roosevelt Hot Springs geothermal power plant does not appear to correlate with current pumping histories. The Zandt swarm area continues to be characterized by seismic swarm activity. While many new events have been added to the catalog, I concur with Zandt et al. (1982) who concluded that this region is an area with low magnitude events and low seismic rates punctuated by low magnitude seismic swarms. This work has lowered the magnitude of completeness to 1.5 and provides the seismic baseline necessary for the FORGE project's induced seismicity mitigation plan.

REFERENCES CITED

Allis, R., Gwynn, M., Hardwick, C., Kirby, S., Moore, J., Chapman, D., 2015. Re-evaluation of the Pre-Development Thermal Regime of Roosevelt Hydrothermal System , Utah. Fourtieth Work. Geotherm. Reserv. Eng. Stanford Univ.

Allis, R., Larsen, G., Survey, U.G., Energy, P., City, S.L., 2012. Roosevelt Hot Springs Geothermal Field, Utah - Reservoir Response After More Than 25 Years of Power Production. Proceedings, Thirty-Seventh Work. Geotherm. Reserv. Eng.

Arabasz, W.J., Burlacu, R., Pnakow, K.L., 2007. An Overview of Historical and Contemporary Seismicity in Central Utah. UGA Publ. 36.

Arabasz, W.J., Pechmann, J.C., Burlacu, R., 2016. A Uniform Moment Magnitude Earthquake Catalog and Background Seismisity Rates for the Wasatch Front and Surrounding Utah Region: Appendix E in Working Group on Utah Earthquake Probabilities (WGUEP). Earthq. Probab. Wasatch Front Reg. Utah, Idaho, Wyoming Utah Geol. Surv. Misc. Publ. 16-3 variously paginated.

Barker, C.A., 1986. Upper-Crustal Structure of the Milford Valley and Roosevelt Hot Springs, Utah Region, by Modeling of Seismic Refreaction and Reflection Data.

Barrett, S. A., Beroza, G.C., 2014. An Empirical Approach to Subspace Detection. Seismol. Res. Lett. 85, 594-600. doi:10.1785/0220130152

Ben-Zion, Y., Allam, A.A., 2013. Seasonal Thermoelastic Strain and Postseismic Effects in Parkfield Borehole Dilatometers. Earth Planet. Sci. Lett. 379, 120-126. doi:10.1016/j.epsl.2013.08.024

Bowers, D., Marmo, B., Selby, N., Buckingham, M.-P., Styles, P., Toon, S., 2015. Seismic Vibrations from Wind Turbines and Their Effects on the Seismometer Array at Eskdalemuir. AWE Presentation. 1-25.

Brogan, G.E., Birkhahn, P.C., 1982. Faults and Occurrence of Geothermal Anomalies.

Chambers, D.J.A., Koper, K.D., Pankow, K.L., Mccarter, M.K., 2015. Detecting and Characterizing Coal Mine Related Seismicity in the Western U. S. Using Subspace Methods 1388-1399. doi:10.1093/gji/ggv383

Coleman, D.S., Walker, J.D., 1994. Modes of Tilting During Extensional Core Complex Development Authors: Drew S . Coleman and J . Douglas Walker Published by : American Association for the Advancement of Science Stable URL : http://www.jstor.org/stable/2882380 JSTOR is a not-for-profi. Science (80-.). 263,

215-218.

Coleman, D.S., Walker, J.D., 1992. Evidence for the Generation of Juvenile Granitic Crust During Continental Extension, Mineral Mountains Batholith, Utah. J. Geophys. Res. Solid Earth 97, 11011-11024. doi:10.1029/92JB00653

Deichmann, N., Giardini, D., 2009. Earthquakes Induced by the Stimulation of an Enhanced Geothermal System below Basel (Switzerland). Seismol. Res. Lett. 80, 784-798. doi:10.1785/gssrl.80.5.784

Deichmann, N., Kraft, T., Evans, K.F., 2014. Identification of Faults Activated During the Stimulation of the Basel Geothermal Project from Cluster Analysis and Focal Mechanisms of the Larger Magnitude Events. Geothermics 52, 84-97. doi:10.1016/j.geothermics.2014.04.001

Estrella, H.F., Korn, M., Alberts, K., 2017. Analysis of the Influence of Wind Turbine Noise on Seismic Recordings at Two Wind Parks in Germany. J. Geosci. Environ. Prot. doi:10.4236/gep.2017.55006

Evans, K.F., Zappone, A., Kraft, T., Deichmann, N., Moia, F., 2012. A Survey of the Induced Seismic Responses to Fluid Injection in Geothermal and CO2 Reservoirs in Europe. Geothermics 41, 30-54. doi:10.1016/j.geothermics.2011.08.002

Faulder, D.D., 1991. Conceptual Geologic Model and Native State Model of the Roosevelt Hot Springs Hydrothermal System. Sixt. Work. Geotherm. Reserv. Eng. SGP-TR-134, 131-142.

Gammans, C., 2013. Low-Angle Normal Faulting in the Basin and Range-Colorado Plateau Transition Zone During the Janurary 3, 2011 Circleville, UT Earthquake Sequence. Dep. Geol. Geophys. Univ. Utah, Master's Thesis 1-69.

Gibbons, S.J., Ringdal, F., 2006. The Detection of Low Magnitude Seismic Events Using Array-Based Waveform Correlation. Geophys. J. Int. 165, 149-166. doi:10.1111/j.1365-246X.2006.02865.x

Grünthal, G., 2014. Induced Seismicity Related to Geothermal Projects Versus Natural Tectonic Earthquakes and Other Types of Induced Seismic Events in Central Europe. Geothermics 52, 22-35. doi:10.1016/j.geothermics.2013.09.009

Hainzl, S., 2004. Seismicity Patterns of Earthquake Swarms Due to Fluid Intrusion and Stress Triggering. Geophys. J. Int. 159, 1090-1096. doi:10.1111/j.1365-246X.2004.02463.x

Harris, D.B., 2006. Subspace Detectors : Theory UCRL-TR-222758; 48. doi:10.2172/900081

Harris, D.B., Paik, T., 2006. Subspace Detectors : Efficient Implementation. Lawrence Livermore Natl. Lab. 36.

Heinzel, G., Rüdiger, a, Schilling, R., Hannover, T., 2002. Spectrum and Spectral

Density Estimation by the Discrete Fourier Transform (DFT), Including a Comprehensive List of Window Functions and Some New Flat-Top. Max Plank Inst. 1-84. doi:395068.0

Koper, K.D., Burlacu, R., 2015. The Fine Structure of Double-Frequency Microseisms Recorded by Seismometers in North America. J. Geophys. Res. Solid Earth 120, 1-15. doi:10.1002/2014JB011820.Received

Kreemer, C., Blewitt, G., Hammond, W.C., 2010. Evidence for an Active Shear Zone in Southern Nevada Linking the Wasatch Fault to the Eastern California Shear Zone. Geology 38, 475-478. doi:10.1130/G30477.1

Leys, C., Ley, C., Klein, O., Bernard, P., Licata, L., 2013. Detecting Outliers: Do Not Use Standard Deviation Around the Mean, Use Absolute Deviation Around the Median. J. Exp. Soc. Psychol. 49, 764-766. doi:10.1016/j.jesp.2013.03.013

McNamara, D.E., Buland, R.P., 2004. Ambient Noise Levels in the Continental United States. Bull. Seismol. Soc. Am. 94, 1517-1527. doi:10.1785/012003001

Michelini, A., Bolt, B.A., 1986. Application of the Principal Parameters Method to the 1983 Coalinga, California, Aftershock Sequence. Bull. Seismol. Soc. Am. 76 (2), 409-420.

Moore, J., Allis, R., Wannamaker, P., McLennan, J., Barker, B., Davatzes, N., Hardwick, C., Lowe, M., Kirby, S., Lockner, D., Miller, J., Milligan, M., Nash, G., Pankow, K., Podgorney, R., Rickard, W., Rose, P., Simmons, S., Weaver, L., Winkler, D., 2014. Enhanced Geothermal System Testing And Development at The Milford, Utah Forge Site., Department of Energy Report, Control Number: 0890-1503

Mukuhira, Y., Asanuma, H., Niitsuma, H., Häring, M.O., 2013. Characteristics of Large-Magnitude Microseismic Events Recorded During and After Stimulation of a Geothermal Reservoir at Basel, Switzerland. Geothermics 45, 1-17. doi:10.1016/j.geothermics.2012.07.005

Nielson, D.L., Evans, S.H., Sibbett, B.S., 1986. Magmatic, Structural, and Hydrothermal Evoution of the Mineral Mountains Intrusive Complex, Utah. Geol. Soc. Am. Bull. 97, 765-777.

Nielson, D.L., Sibbett, B.S., McKinney, D.B., Hulen, J.B., Moore, J.N., Samberg, S.M., 1978. Geology of Roosevelt Hot Springs KGRA, Beaver County, Utah, Earth Science Laboratory.

Pankow, K.L., Arabasz, W.J., Pechmann, J.C., Nava, S.J., 2004. Triggered Seismicity in Utah from the 3 November 2002 Denali Fault Earthquake 94, 332-347.

Pankow, K.L., Moore, J.R., Mark Hale, J., Koper, K.D., Kubacki, T., Whidden, K.M., McCarter, M.K., 2014. Massive Landslide at Utah Copper Mine Generates Wealth of Geophysical Data. GSA Today 24, 4-9. doi:10.1130/GSATG191A.1

Pechmann, J.C., Arabasz, W.J., Pankow, K.L., Jensen, M.E., 2002. Seismic Velocity Model for the Trail Mountain Area. Appendix B in, in: Arabasz, Walter, J., Nava, J., Mccarter, M.K., Pankow, K.L., Pechmann, J.C., Jensen, M.E., McKinzie, J.D. (Eds.), Ground-Motion Recording and Analysis of Mining-Induced Seismcity in the Trail Mountain Area, Emery County, Utah. pp. B1-B9.

Peterson, J., 1993. Observations and Modeling of Seismic Background Noise. U.S. Geol. Surv. Open File Rep. 93-322.

Plenkers, K., Ritter, J.R.R., Schindler, M., 2013. Low Signal-to-Noise Event Detection Based on Waveform Stacking and Cross-Correlation: Application to a Stimulation Experiment. J. Seismol. 17, 27-49.

Prowell, I., Elgamal, A., Jonkman, J., 2010. FAST Simulation of Wind Turbine Seismic Response. 2009 Asian-Pacific Netw. Centers Earthq. Eng. Res. Work.

Robinson, R., Iyer, H.M., 1981. Delineation of a Low-Velocity Body Under the Roosevelt Hot Springs Geothermal Area , Utah , Using Teleseismic P-Wave Data. Springs 46, 1456-1466.

Schaff, D.P., Waldhauser, F., 2005. Waveform Cross-Correlation-Based Differential Travel-Time Measurements at the Northern California Seismic Network. Bull. Seismol. Soc. Am. 95, 2446-2461. doi:10.1785/0120040221

SCPPA, 2017. Milford Wind Corridor Phase I and II [WWW Document]. South. Calif. Public Power Auth. URL http://www.scppa.org/page/Milford-Wind

Shearer, P.M., Hardebeck, J.L., Astiz, L., Richards-Dinger, K.B., 2003. Analysis of Similar Event Clusters in Aftershocks of the 1994 Northridge, California, Earthquake. J. Geophys. Res. Earth 108, 14. doi:2035\r10.1029/2001jb000685

Shelly, D.R., Hill, D.P., Massin, F., Farrell, J., Smith, R.B., Taira, T., 2013. A Fluid-Driven Earthquake Swarm on the Margin of the Yellowstone Caldera. J. Geophys. Res. E Planets 118, 4872-4886. doi:10.1002/jgrb.50362

Sibbett, B.S., Nielson, D.L., 1980. Geology of the Central Mineral Mountains Beaver County, Utah.

Smith, R.B., Arabasz, W.J., 1991. Seismicity of the Intermountain Seismic Belt, in: Slemmons, D.B., Engdahl, E.R., Zoback, M.D., Blackwell, D.D. (Eds.), Neotectonics of North America: Geological Society of America Decade of North American Geology, Map 1, Scale: 1:5,000,000. pp. 185-228. doi:10.1130/DNAG-CSMS-NEO.185

Smith, R.B., Bruhn, R.L., 1984. Intraplate Extensional Tectonics of the Eastern Basin-Range, Inferences on Structural Style from Seismic Reflection Data, Regional Tectonics, and Thermal-Mechanical Models of Brittle-Ductile Defromation. JGR 89, 5733-5762.

Stein, J.R., 2016. Seismic Source Discriminination in the Wasatch Plateau Region.

Stein, S., Wysession, M., 2003. An Introduction to Seismology, Earthquakes, and Earth Structure.

Terakawa, T., Miller, S.A., Deichmann, N., 2012. High Fluid Pressure and Triggered Earthquakes in the Enhanced Geothermal System in Basel, Switzerland. J. Geophys. Res. Solid Earth 117, 1-15. doi:10.1029/2011JB008980

Trugman, D.T., Shearer, P.M., 2017. GrowClust: A Hierarchical Clustering Algorithm for Relative Earthquake Relocation, with Application to the Spanish Springs and Sheldon, Nevada, Earthquake Sequences. Seismol. Res. Lett. 88, 379-391. doi:10.1785/0220160188

Tsai, V.C., 2011. A Model for Seasonal Changes in GPS Positions and Seismic Wave Speeds Due to Thermoelastic and Hydrologic Variations. J. Geophys. Res. Solid Earth 116, 1-9. doi:10.1029/2010JB008156

Ward, S.H., Parry, W.T., Nash, W.P., Sill, W.R., Cook, K.L., Smith, R.B., Chapman, D.S., Brown, F.H., Whelan, J.A., Bowman, J.R., 1987. A Summary of Geology, Geochemistry, and Geophysics of the Roosevelt Hot Springs Thermal Area, Utah. Geophysics 43, 1515-1542.

Whidden, K.M., Pankow, K.L., 2012. A Catalog of Regional Moment Tensors in Utah from 1998 to 2011. Seismol. Res. Lett. 83, 775-783. doi:10.1785/0220120046

Zandt, G., McPherson, L., Schaff, S., Olsen, S., 1982. Seismic Baseline and Induciton Studies; Roosevelt Host [sic] Springs, Utah and Raft River, Idaho. Earth Sci. Lab.

Zang, A., Oye, V., Jousset, P., Deichmann, N., Gritto, R., McGarr, A., Majer, E., Bruhn, D., 2014. Analysis of Induced Seismicity in Geothermal Reservoirs - An Overview. Geothermics 52, 6-21. doi:10.1016/j.geothermics.2014.06.005